

## HOT ELECTROMAGNETIC OUTFLOWS II: JET BREAKOUT

MATTHEW RUSSO

Department of Physics, University of Toronto, 60 St. George St., Toronto, ON M5S 1A7, Canada.

CHRISTOPHER THOMPSON

Canadian Institute for Theoretical Astrophysics, 60 St. George St., Toronto, ON M5S 3H8, Canada.

*Submitted to The Astrophysical Journal*

### ABSTRACT

We consider the interaction between radiation, matter and a magnetic field in a compact, relativistic jet. The entrained matter accelerates outward as the jet breaks out of a star or other confining medium. In some circumstances, such as gamma-ray bursts (GRBs), the magnetization of the jet is greatly reduced by an advected radiation field while the jet is optically thick to scattering. Where magnetic flux surfaces diverge rapidly, a strong outward Lorentz force develops and radiation and matter begin to decouple. The increase in magnetization is coupled to a rapid growth in Lorentz factor. We take two approaches to this problem. The first examines the flow outside the fast magnetosonic critical surface, and calculates the flow speed and the angular distribution of the radiation field over a range of scattering depths. The second considers the flow structure on both sides of the critical surface in the optically thin regime, using a relaxation method. In both approaches, we find how the terminal Lorentz factor, and radial profile of the outflow, depend on the radiation intensity and optical depth at breakout. The effect of bulk Compton scattering on the radiation spectrum is calculated by a Monte Carlo method, while neglecting the effects of internal dissipation. The peak of the scattered spectrum sits near the seed peak if radiation pressure dominates the acceleration, but is pushed to a higher frequency if the Lorentz force dominates, and especially if the seed photon cone is broadened by interaction with a slower component of the outflow.

*Subject headings:* MHD — plasmas — radiative transfer — scattering — gamma rays: stars

### 1. INTRODUCTION

Gamma-ray bursts involve collimated, relativistic outflows, as deduced from their rapid variability, extreme apparent energies (which can exceed the binding energy of a neutron star: Kulkarni et al. 1999; Amati et al. 2002), and the expected presence of non-relativistic material surrounding the engine. The jet is heated as it works through this denser material, which may represent a stellar envelope (Woosley 1993; Paczynski 1998), or neutron-rich debris from a binary neutron star merger (e.g. Dessart et al. 2009). As a result, a nearly blackbody radiation field may carry a significant fraction of the energy flux near the point of breakout.

We focus here on strongly magnetized jets that are driven outward by a combination of the Lorentz force, and the force of radiation scattering off ionized matter. The acceleration of such a ‘hot electromagnetic outflow’ (Thompson 1994; Meszaros & Rees 1997; Drenkhahn & Spruit 2002; Thompson 2006; Giannios & Spruit 2007; Zhang & Yan 2011), in which radiation pressure dominates matter pressure, has been treated quantitatively in Russo & Thompson (2012) (Paper I) in the approximation that the poloidal magnetic field lines threading the outflow are radial and monopolar. The radiation field is self-collimating outside the scattering photosphere, but may continue to interact with slower material that it entrained by the jet. In Paper I, the outflow was followed both inside and outside the fast magnetosonic critical point. The radiation force is especially important outside the fast point: even where the kinetic energy flux of the entrained charged particles is small compared with the magnetic Poynting flux, they provide an efficient couple between magnetic field and radiation. The relative influence of the two stresses on the asymptotic Lorentz factor depends on the radiation compactness. Generally, the importance of radiation pressure is enhanced by bulk relativistic motion at the photosphere.

In this paper we generalize the calculation of Paper I to include non-spherical effects. A magnetized outflow experiences a strong Lorentz force where poloidal flux surfaces in the jet diverge from each other faster than in a monopolar geometry (Camenzind 1987; Li et al. 1992b; Begelman & Li 1994; Vlahakis & Königl 2003a,b; Beskin & Nokhrina 2006; Tchekhovskoy et al. 2009). In particular, a magnetized jet accelerates rapidly when it breaks out of the confining material (Tchekhovskoy et al. 2010). The simulations in that paper demonstrated the effect for a cold magnetohydrodynamic (MHD) outflow, but did not include the effects of radiation pressure and drag.

The magnetization of a hot electromagnetic outflow remains modest inside its scattering photosphere, where the radiation is tied to the matter, and the radiation enthalpy contributes to the inertia. Our first task in this paper is, therefore, to examine how the radiation field begins to decouple from the matter when the jet material breaks out. We define a bulk frame in which the radiation force vanishes, by taking angular moments of the radiation field, and then track the proportions of the energy flux carried by matter, radiation, and magnetic field, at both large and small optical depths.

Given the flow profile so obtained, the radiation spectrum is calculated by a Monte Carlo method. Here we focus on the effects of bulk Compton scattering, which provide a direct probe of the outflow dynamics. We neglect the effects of internal dissipation by various process such as MHD wave damping, magnetic reconnection, or shocks.

The second principal goal of this paper is to obtain the longitudinal motion along a magnetic flux surface, taking into account

both the radiation force and the singularity in the flow equations which appears at the fast point. Our focus here is on the zone near and outside the transparency surface; previous efforts to calculate the effect of pressure gradient forces on relativistic outflows (e.g. Vlahakis & Königl 2003b) have focused on the optically thin regime. We argued in Paper I that the effect of a magnetic pressure gradient driven by internal reconnection (Drenkhahn & Spruit 2002) has been overestimated, because it neglects the addition to the outflow inertia from particle heating and a strong non-radial magnetic field.

Coupled wind equations for the matter Lorentz factor and angular momentum are derived in an arbitrary poloidal field geometry, restricted to the case of small angles near the rotational axis, but allowing for arbitrary relative flaring of the flux surfaces. The fast point generally sits close to the breakout surface of the jet. Our main simplification of the problem is to impose a particular shape for the poloidal flux surfaces, and not to solve self-consistently for the cross-field force balance. Two constraints are applied to the imposed magnetic field profile: that the rate of flaring is causal, and that the transverse component of the radiation force is at most a perturbation to the transverse Lorentz force.

The plan of this paper is as follows. Section 2 reviews the acceleration of a relativistic MHD outflow driven by the differential flaring of magnetic flux surfaces, and considers the radiation transfer equation in the limit of small angles. Equations are derived for the acceleration of a steady MHD outflow outside its fast point, in combination with the radial evolution of the magnetization, radiation energy flux, scattering depth, and the frame in which the radiation force vanishes. These equations are solved in particular cases relevant to GRB jets. Section 3 presents a simple model of a spreading thin jet outside its photosphere, and derives the corresponding steady flow equations for arbitrary radiation force and magnetization. The effect of radiation pressure on the fast point is considered analytically, and numerical solutions for the flow both inside and outside the fast point are presented. Section 4 describes Monte Carlo calculations of the emerging radiation spectrum in both the causal jet model of Section 2, and the optically thin model of Section 3. Section 5 summarizes our results. The Appendix presents a derivation of the radiation force in a thin, transparent jet.

## 2. FLARING, HOT MAGNETIZED JET: TRANSITION TO LOW OPTICAL DEPTH (MODEL I).

We consider a stationary, axisymmetric outflow of perfectly conducting material that is tied to a very strong magnetic field. The outflow is also a strong source of radiation, which scatters off the advected light particles (electrons as well as positrons). Matter pressure gradients are neglected in comparison with inertial and Lorentz forces as well as the radiation force.

We start by considering the exchange of energy between different components of the outflow. Deviations from radial motion are assumed to be small compared with the angular width of the photon beam: that is, the interaction between matter and radiation

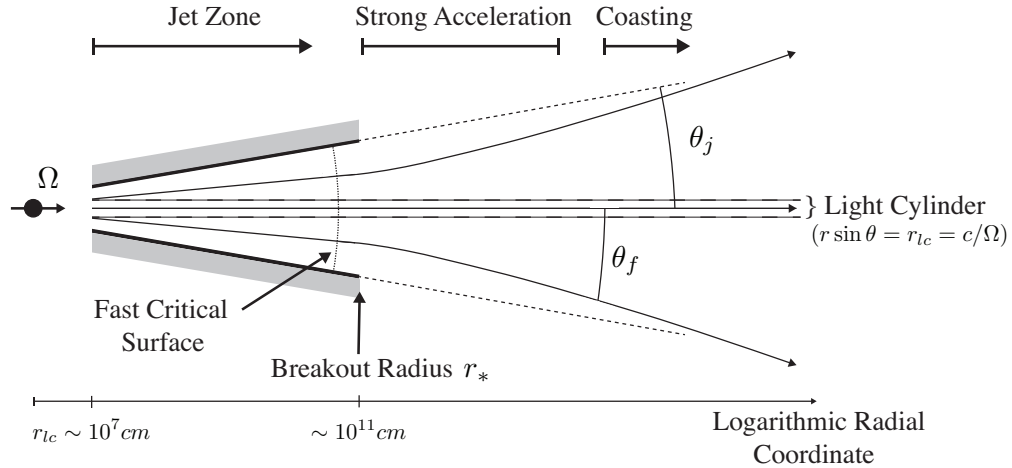


FIG. 1.— Geometry and approximate scale of the flow solutions for jet model I.

is calculated assuming radial matter motion, but allowance is made for strong radial Lorentz forces driven by a small amount of magnetic field line flaring. The beam angular width is set, more or less, by the Lorentz factor of the outflow at its transparency surface. Here allowance is made for a finite optical depth of the magnetofluid. By taking angular moments of the radiation field, we track the difference between the Lorentz factor of the matter, and of the frame in which the radiation force vanishes, as the

matter is accelerated by a strong Lorentz force. This approach is suited to a single-component magnetofluid, but also allows for the presence of a second, slower component that scatters the radiation field into a broader cone, and plausibly is present in GRBs (Paper I).

Given the complications introduced by a finite optical depth, we now consider only supermagnetosonic outflows. In a second approach (Section 3), we account for non-radial matter motion and follow the flow across the fast critical surface, but restrict the calculation to low optical depth. The geometry of the model is shown in Figure 6. After being launched by the central engine (with angular frequency  $\Omega$ ) the flow enters the jet zone along the rotation axis. We ignore the details of the acceleration while the jet is still very optically thick, and laterally confined. Our calculation begins a short distance inside breakout (at radius  $r_*$ ), by which point the flow is assumed to be supermagnetosonic. Outside breakout, transverse pressure support effectively vanishes and field lines begin to diverge differentially. The outward Lorentz force increases dramatically over a narrow range of radius, until a loss of causal contact across the jet forces the flow lines to straighten out, and the acceleration is cut off. Although the scattering photosphere could, in principal, sit anywhere in the outflow, breakout is associated with a large drop in optical depth. In our calculations, the photosphere therefore usually sits just outside breakout. Low optical depth at breakout does produce an interesting imprint of bulk Compton scattering on the emergent spectrum (Section 4).

### 2.1. Exchange of Energy between Radiation and Magnetofluid

We consider the flow along a poloidal magnetic field line  $\theta_f(r)$ , starting at a large enough radius that the streamline sits well outside the light cylinder of the central engine. Deviations from radial motion are neglected, except in so far that they influence the radial Lorentz force. Then the outflow has a fixed total luminosity per sterad, including contributions from matter, magnetic field, and radiation,

$$\frac{dL}{d\Omega} = \frac{dL_k}{d\Omega} + \frac{dL_p}{d\Omega} + \frac{dL_\gamma}{d\Omega} = \text{const.} \quad (1)$$

Here

$$\frac{1}{r^2} \frac{dL_k}{d\Omega} = \Gamma c^2 \cdot \Gamma \rho v_p = \frac{\Gamma c^2}{r^2} \frac{d\dot{M}}{d\Omega} \quad (2)$$

is the kinetic energy flux of material of proper density  $\rho$ , poloidal (radial) speed  $v_p$ , and Lorentz factor  $\Gamma$ . The poloidal Poynting flux is expressed in terms of the electric and magnetic vectors  $\mathbf{E}$ ,  $\mathbf{B}$  by

$$\frac{1}{r^2} \frac{dL_p}{d\Omega} = \hat{B}_p \cdot \frac{\mathbf{E} \times \mathbf{B}}{4\pi} c. \quad (3)$$

Substituting  $\mathbf{E} = -\mathbf{v} \times \mathbf{B}/c$  into the induction equation gives  $\partial \mathbf{B}/\partial t = \nabla \times (\mathbf{v} \times \mathbf{B})$ , where  $\mathbf{v}$  is the fluid velocity. The steady solution to this equation involves the pattern angular velocity  $\Omega_f$  of the magnetic field, which is constant along a poloidal flux surface. It relates the toroidal components of  $\mathbf{B}$  and  $\mathbf{v}$  via

$$B_\phi = \frac{v_\phi - \Omega_f r \sin \theta_f}{v_p} B_p. \quad (4)$$

Substituting this into (3) gives

$$\frac{1}{r^2} \frac{dL_p}{d\Omega} = -\Omega_f r \sin \theta_f \frac{B_p B_\phi}{4\pi}. \quad (5)$$

Far outside the light cylinder, the outflow rotates slowly and the magnetic field is predominantly toroidal:  $v_\phi \ll v_p \simeq c$  and  $|B_\phi| \gg |B_p|$ . Hence

$$\frac{1}{r^2} \frac{dL_p}{d\Omega} \simeq (\Omega_f r \sin \theta_f)^2 \frac{B_p^2}{4\pi c}. \quad (6)$$

It is useful to normalize all components of the energy flux to the poloidal mass flux, which is conserved along a poloidal flux surface in a steady MHD wind,  $d\dot{M}/d\Phi_p = \Gamma \rho v_p / B_p = \text{const.}$  Assuming further that  $\Gamma \gg 1$ , the magnetization becomes

$$\sigma = \frac{dL_p/d\Omega}{(d\dot{M}/d\Omega)c^2} \simeq \frac{(\Omega_f r \sin \theta_f)^2 B_p}{4\pi c^3} \frac{B_p}{\Gamma \rho v_p} \Big|_*, \quad (7)$$

The radius  $r_*$  and the label  $*$  denote a position in the jet where the confining medium changes rapidly, e.g. the jet moves beyond the photosphere of a Wolf-Rayet star. (We will distinguish this from an inner boundary  $r_i$  for the jet integration, which typically is set just interior to the breakout radius.) Taking  $r_* \gg c/\Omega_f$ ,

$$\frac{\sigma}{\sigma_*} = \frac{(r \sin \theta_f)^2 B_p}{(r \sin \theta_f)_*^2 B_{p*}}. \quad (8)$$

(Note that our definition of  $\sigma$  differs by a factor  $\Gamma$  from the one used by Tchekhovskoy et al. 2009 in a similar derivation.) Defining the normalized photon luminosity by

$$\mathcal{R} = \frac{dL_\gamma/d\Omega}{(d\dot{M}/d\Omega)c^2}, \quad (9)$$

the equation of energy conservation (1) can be written

$$\Gamma - \Gamma_* = -(\sigma - \sigma_* + \mathcal{R} - \mathcal{R}_*). \quad (10)$$

Note that  $\mathcal{R}$  is related to the photon compactness and the scattering depth measured outward from radius  $r$  by

$$\chi \equiv \frac{\sigma_T}{\bar{m}c^3} \frac{dL_\gamma}{d\Omega} \sim (2-6)\Gamma^2\tau_{\text{es}}\mathcal{R}, \quad (11)$$

where  $\sigma_T$  is the Thomson cross section and  $\bar{m}$  is the material inertia per scattering charge. The coefficient here depends on the acceleration of the outflow, as can be seen from the expression for the optical depth of a (radially moving) photon

$$\tau_{\text{es}}(r) = \alpha_{\text{es}}(r) \int_r^\infty [1 - \beta(r')] \frac{r'^2 dr'}{\beta(r')r'^2}; \quad \beta(r) \equiv \frac{v}{c} \simeq \frac{v_r}{c} \quad (12)$$

[see equation (26) for notation]. The coefficient is  $\sim 2$  when the Lorentz factor is constant and reaches  $\sim 6$  for a linear growth,  $\Gamma \propto r$ .

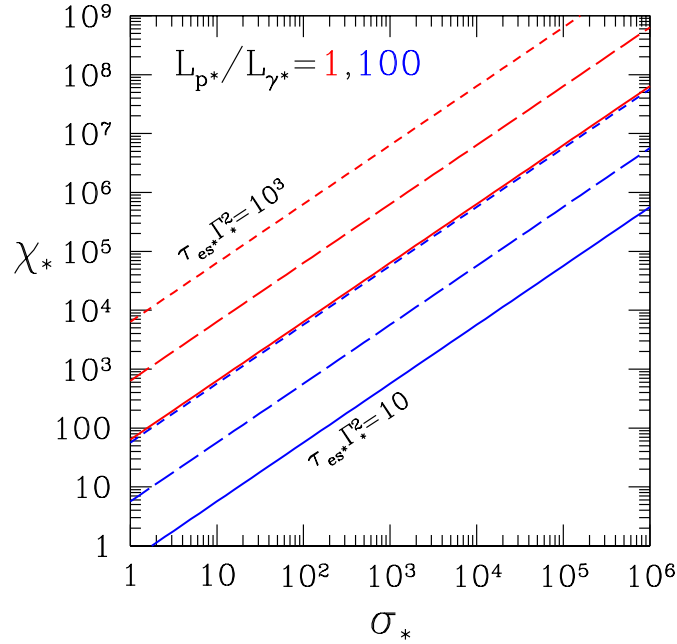


FIG. 2.— Radiation compactness at breakout for different ratios of Poynting to radiation flux: 1 (red), 100 (blue). Rescaled scattering optical depth  $\tau_{\text{es}*}\Gamma_*^2 = 10, 10^2, 10^3$  is plotted as solid, long-dashed and short-dashed respectively. The compactness drops below these curves beyond the breakout point. Strong radiative driving increases the Lorentz factor above the photospheric value  $\Gamma(r_\tau)$  if  $\chi_* \gtrsim \Gamma(r_\tau)^3$ .

## 2.2. Importance of Radiative Driving in Outflows with a Relativistically Moving Photosphere

Jets of a high magnetization can encounter a scattering photosphere not too far outside breakout from a confining medium such as a Wolf-Rayet envelope or neutron-rich debris cloud. Let us take a fiducial luminosity  $4\pi dL_\gamma/d\Omega = 10^{51} L_{51} \text{ erg s}^{-1}$  and a deconfinement radius  $r_* = 10^{10} r_{*,10} \text{ cm}$ . The corresponding compactness (11) is  $\chi_* = 1 \times 10^8 L_{51} r_{*,10}^{-1} (m_p/\bar{m})$ . Since the Lorentz factor increases rapidly after breakout due to MHD stresses, we fix  $r$  and then consider the condition for a photosphere to emerge at a radius  $r_\tau \gtrsim r_*$ . This corresponds to  $\Gamma^2(r_\tau)\mathcal{R}(r_\tau) \sim 10^7 (m_p/\bar{m})$ . For example, if the jet is hot and strongly magnetized,  $\mathcal{R} \sim \sigma \sim 10^5$ , and pairs have largely annihilated within the bulk of the jet material, then the photosphere emerges at  $\Gamma(r_\tau) \sim 10$ .

The radiation field is capable of driving a light baryonic outflow to a terminal Lorentz factor (see Section 2 of Paper I),

$$\Gamma_\infty \sim [\Gamma(r_\tau)\chi(r_\tau)]^{1/4}. \quad (13)$$

Moderately relativistic motion at the photosphere enhances  $\Gamma_\infty$  and, as we now motivate, a larger radiation compactness. When the Lorentz force is taken into account self-consistently,  $\Gamma_\infty$  can be greater or smaller than (13), as we detail in this paper.

An upper limit on the photon compactness is derived by demanding that the fluid be optically thin at breakout,  $\tau_{\text{es}}(r_*) \leq 1$ . Then the photosphere sits at  $r_\tau < r_*$ , and the compactness (11) at breakout is

$$\chi_* = \frac{r_\tau}{r_*} \chi(r_\tau) \simeq 6 \frac{r_\tau}{r_*} \Gamma^2(r_\tau) \frac{dL_{\gamma*}/d\Omega}{(dM/d\Omega)c^2}. \quad (14)$$

Hence  $\Gamma_\infty \propto \Gamma(r_\tau)^{3/4}$  in a jet of a fixed  $\mathcal{R}$ . The radiation flux at breakout is below the Poynting flux if

$$\chi_* \lesssim 6 \frac{r_\tau}{r_*} \Gamma^2(r_\tau) \sigma_*. \quad (15)$$

In Figure 2 we relate the compactness, magnetization and optical depth at breakout for different ratios of Poynting to radiation flux.

The aforementioned hot jet moving at  $\Gamma(r_\tau) \sim 10$  at its photosphere, with a magnetization  $\sigma \sim \mathcal{R} \sim 10^5$ , can be pushed by radiation pressure up to a terminal Lorentz factor  $\Gamma_\infty \sim (1 \times 10^9)^{0.25} \sim 200$ . More relativistic material accelerated by the Lorentz force will, alternatively, feel a retarding force from the radiation field.

### 2.3. Cold MHD Flow without Radiation Pressure

To begin, we review the case where photons are absent, and assume a thin jet in which the magnetic field lines have poloidal angle  $\theta_f \ll 1$ . Only a small differential bending of the field lines is needed to push a cold magnetofluid to large  $\Gamma$ : their polar angle must deviate from conical geometry by  $\delta\theta_f/\theta_f \sim \Gamma/\sigma$ . A basic constraint on the rate of bending is obtained if the transverse component of the Lorentz force in the matter rest frame is limited to

$$\frac{1}{c} \left| \mathbf{J}' \times \mathbf{B}' - \beta \cdot (\mathbf{J}' \times \mathbf{B}') \frac{\beta}{\beta^2} \right| \lesssim \frac{B_\phi^2}{4\pi r/\Gamma}. \quad (16)$$

The prime ' denotes the rest frame, in which  $r/\Gamma$  is a characteristic causal distance, and  $\beta \equiv \mathbf{v}/c$ . Then

$$r \frac{d(\delta\theta_f)}{dr} \lesssim \frac{1}{\Gamma}, \quad (17)$$

so that typically  $\delta\theta_f \sim 1/\Gamma$ . This is seen in the dynamic cold MHD calculations of Tchekhovskoy et al. (2009), where strong Lorentz forces are generated in a narrow fan near the jet edge.

Conservation of magnetic flux implies that  $B_p r^2 \theta_f d\theta_f = \text{const}$ . Hence, writing  $\theta_f = \theta_f(r_*) + \delta\theta_f \equiv \theta_{f*} + \delta\theta_f$ , equation (8) becomes

$$\sigma = \sigma_* \left[ 1 - \frac{d(\delta\theta_f/\theta_{f*})}{d \ln \theta_{f*}} \right]. \quad (18)$$

The change in the ratio of Poynting and mass fluxes can then be written

$$\frac{1}{\sigma_*} \frac{d\sigma}{dr} = -\theta_{f*} \frac{d}{d\theta_{f*}} \left( \frac{K}{\Gamma \theta_{f*} r} \right). \quad (19)$$

The envelope function  $K(\theta_f) \sim 1$  away from the jet axis, and vanishes on the axis given the assumption of axisymmetry.

### 2.4. Radiation Force

Given the relativistic motion of the matter, the radiation field can be assumed to interact with it via Thomson scattering. In a frame where the matter moves with velocity  $\beta c$ , and a photon has wave vector  $\mathbf{k} = k\hat{\mathbf{k}}$ , a scattering charge feels a force

$$\mathbf{F}^{\text{rad}} = \frac{\sigma_T I}{c} \int \left( 1 - \beta \cdot \hat{\mathbf{k}} \right) \left[ \hat{\mathbf{k}} - \beta \Gamma^2 \left( 1 - \beta \cdot \hat{\mathbf{k}} \right) \right] d\Omega. \quad (20)$$

Here  $I(\mu) = \int d\nu I_\nu$  is the spectral intensity integrated over frequency, and  $\mu$  is the direction cosine  $\mu = \cos(\theta) = \hat{\mathbf{k}} \cdot \hat{\mathbf{r}}$ .

It is useful to define angular moments of  $I$ ,

$$F_n \equiv 2\pi \int d\mu (1 - \mu)^n I(\mu) \equiv 2\pi \int (\Delta\mu)^n I(\Delta\mu), \quad (21)$$

so that for a narrow beam,  $\Delta\mu \simeq \frac{1}{2}\theta^2 \ll 1$ , the radiation energy flux is approximately equal to  $F_0 = \mathcal{R} \Gamma \rho c^3$ . We may define a frame moving at Lorentz factor  $\Gamma_{\text{eq}}$  (speed  $\beta_{\text{eq}}$ ) in which the radiation field is nearly isotropic and the radiation force vanishes. Defining the bulk frame radiation energy density by  $u'$ , one has

$$I(\Delta\mu) \simeq \frac{cu'/4\pi}{[\Gamma_{\text{eq}}(1 - \beta_{\text{eq}}\mu)]^4} = \frac{I(0)}{(1 + 2\Gamma_{\text{eq}}^2 \Delta\mu)^4}. \quad (22)$$

Substituting this into (21) yields the relations

$$F_1 = \frac{1}{4\Gamma_{\text{eq}}^2} F_0; \quad F_2 = \frac{1}{\Gamma_{\text{eq}}^2} F_1. \quad (23)$$

Expanding the radiation force (20) in  $\Delta\mu$  gives

$$F_r^{\text{rad}} = \frac{\sigma_T}{4\Gamma^2 c} [F_0 - 4\Gamma^4 F_2] = \frac{\sigma_T F_0}{4\Gamma^2 c} \left[ 1 - \left( \frac{\Gamma}{\Gamma_{\text{eq}}} \right)^4 \right]. \quad (24)$$

The main approximation here is that each field line experiences a small differential bending, so that the bending angle is small compared with  $(2\Delta\mu)^{1/2}$ . This is consistent with rapid acceleration by the Lorentz force near the jet edge (Tchekhovskoy et al. 2010), e.g.  $\delta\theta_f \sim \theta_j - \theta_f \ll \theta_f$ . In the context of GRBs, we can also assume that the flow has propagated far outside the light cylinder, so that  $\beta_\phi \ll 1$  and the toroidal radiation force can be neglected.

### 2.5. Transfer of a Narrow Photon Beam Near a Relativistic Photosphere

We work with the transfer equation in the inertial frame into which the outflow is expanding; a prime denotes the matter rest frame. The radiation transfer equation is written (e.g. Mihalas 1978)

$$\frac{dI_\nu}{ds} = \alpha_{\text{es}}(S_\nu - I_\nu), \quad (25)$$

where

$$\alpha_{\text{es}} = \Gamma(1 - \beta\mu)\alpha'_{\text{es}} = \frac{\Gamma\rho\sigma}{\bar{m}}(1 - \beta\mu) \equiv \frac{\alpha_{\text{es}*}}{\beta(r/r_*)^2}(1 - \beta\mu) \quad (26)$$

is the grey scattering opacity, and

$$S_\nu = \frac{1}{[\Gamma(1 - \beta\mu)]^3} S'_\nu = \frac{1}{2[\Gamma(1 - \beta\mu)]^3} \int d\mu' I'_\nu = \frac{1}{2\Gamma(1 - \beta\mu)^3} \int d\tilde{\mu}(1 - \beta\tilde{\mu})^2 I_{\tilde{\nu}} \quad (27)$$

is the source function in the isotropic scattering approximation. The Doppler relation between unscattered and scattered photon frequencies is  $\tilde{\nu}(1 - \beta\tilde{\mu}) = \nu(1 - \beta\mu)$ , and

$$I'_\nu = [\Gamma(1 - \beta\mu)]^3 I_\nu; \quad d\Omega' = 2\pi d\mu' = \frac{2\pi d\mu}{[\Gamma(1 - \beta\mu)]^2} \quad (28)$$

are the usual transformations. Integrating over frequency gives

$$\frac{dI}{ds} = \alpha_{\text{es}}(S - I); \quad S = \int S_\nu d\nu = \frac{1}{2\Gamma^2(1 - \beta\mu)^4} \int I(\tilde{\mu})(1 - \beta\tilde{\mu})^2 d\tilde{\mu}. \quad (29)$$

Setting  $\Delta\mu \rightarrow 0$ , the path length is  $ds = dr/\mu \simeq dr$ , and one has  $d\Delta\mu/dr \simeq -2\Delta\mu/r$ . Making use of

$$\frac{d}{dr} F_n = -\frac{2(n+1)}{r} \frac{1}{2} \int d\mu(\Delta\mu)^n I + \frac{1}{2} \int d\mu(\Delta\mu)^n \frac{dI}{dr}, \quad (30)$$

gives

$$\frac{1}{r^2} \frac{d}{dr} (r^2 F_0) = -\frac{\alpha_{\text{es}*}}{4\Gamma^2(r/r_*)^2} \left(1 - 4\Gamma^4 \frac{F_2}{F_0}\right) F_0 = -\frac{\alpha_{\text{es}*}}{4\Gamma^2(r/r_*)^2} \left(1 - \frac{\Gamma^4}{\Gamma_{\text{eq}}^4}\right) F_0, \quad (31)$$

and

$$\frac{1}{r^4} \frac{d}{dr} (r^4 F_1) = \frac{\alpha_{\text{es}*}}{8\Gamma^4(r/r_*)^2} \left(1 - \frac{\Gamma^4}{\Gamma_{\text{eq}}^4}\right) F_0, \quad (32)$$

where we have set  $\beta \rightarrow 1$  in the coefficient. These two equations, in combination with (23), allow us to evolve  $\Gamma_{\text{eq}}$  near the scattering photosphere.

The radial evolution of  $\Gamma$  and  $\mathcal{R}$  is obtained by differentiating (10), substituting (19) and (31), and expressing the radiation energy flux in terms of  $\mathcal{R}$ ,

$$r \frac{d\Gamma}{dr} = \sigma_* \frac{d}{d\theta_f} \left(\frac{K}{\Gamma}\right) - r \frac{d\mathcal{R}}{dr}; \quad \frac{d\mathcal{R}}{dr} = -\frac{\alpha_{\text{es}*}}{4\Gamma^2(r/r_*)^2} \left(1 - \frac{\Gamma^4}{\Gamma_{\text{eq}}^4}\right) \mathcal{R}. \quad (33)$$

### 2.6. Numerical Results

Profiles are obtained for  $\Gamma(x)$ ,  $\Gamma_{\text{eq}}(x)$ ,  $R(x)$  and  $\theta_f(x)$  by integrating in the radial dimension. We have made the substitutions  $d/d\theta_f \rightarrow \delta\theta_{\text{gradient}}^{-1}$  and  $K = \theta_{f*}/\theta_j$  in (33). This choice forces the field-line bending to zero near the center of the jet. The gradient angle  $\delta\theta_{\text{gradient}}$  is of the order of  $\theta_j$ , but may be smaller near the edge of the jet as it emerges from a confining medium. For example, the strong acceleration seen near the jet edge in the simulations of Tchekhovskoy et al. (2010) is consistent with  $\delta\theta_{\text{gradient}} \sim \gamma^{-1} \sim 0.1\theta_j$ ; it would presumably be reduced if the jet did not have a sharp edge. In our fiducial model we consider a field line anchored at  $\theta_{f*} = 0.1$ , and take the jet opening half-angle to be  $\theta_j = 0.2$ . To illustrate the effect of jet breakout on the flow parameters, we begin the integration just inside the breakout radius,  $r_i = 0.8r_*$ .

In our first set of integrations, the scattering optical depth is chosen to be large at the breakout radius. At this point, the radiation is still tied to the matter,  $\Gamma_{\text{eq}}(r_*) = \Gamma(r_*)$ , but the rapid MHD acceleration experienced by the flaring jet quickly forces a transition to low  $\tau_{\text{es}}$ . The optical depth for a photon propagating radially from  $r = r_*$  is given by equation (12), and is thus unknown *a priori*. To impose a particular value of  $\tau_{\text{es}}(r_*)$ , we first choose an approximate value of  $\alpha_{\text{es}*}$ , evolve the equations of motion

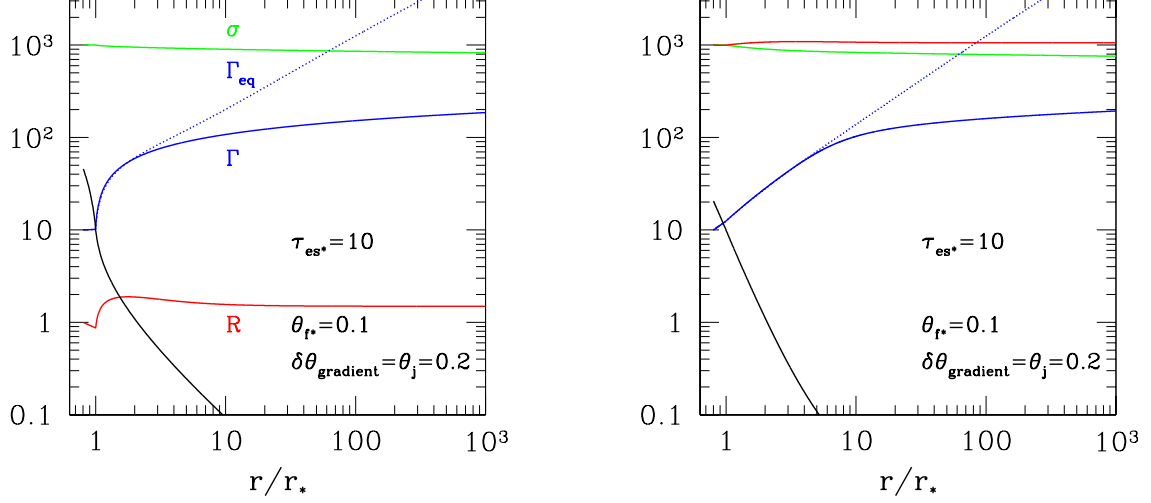


FIG. 3.— Profiles of Lorentz factor  $\Gamma$  (blue), magnetization  $\sigma$  (green), and radiation energy flux  $\mathcal{R}$  (red), in a flaring MHD outflow ( $\sigma_* = 10^3$ ) with radiative driving. The radiation force vanishes in a frame moving with Lorentz factor  $\Gamma_{\text{eq}}$  (dotted blue). Scattering depth integrated from radius  $r$  to infinity (black curve) drops rapidly from  $\tau_{\text{es}*} = 10$  as the flow accelerates. The gradient scale  $\delta\theta_{\text{gradient}}$  sets the relative degree of flaring between neighboring field lines. *Left panel:*  $\mathcal{R}_i = 1$ , *right panel:*  $\mathcal{R}_i = 1000$ . Other parameters:  $r_i = 0.8r_*$ ,  $\Gamma_i = \Gamma_{\text{eq},i} = 10$ .

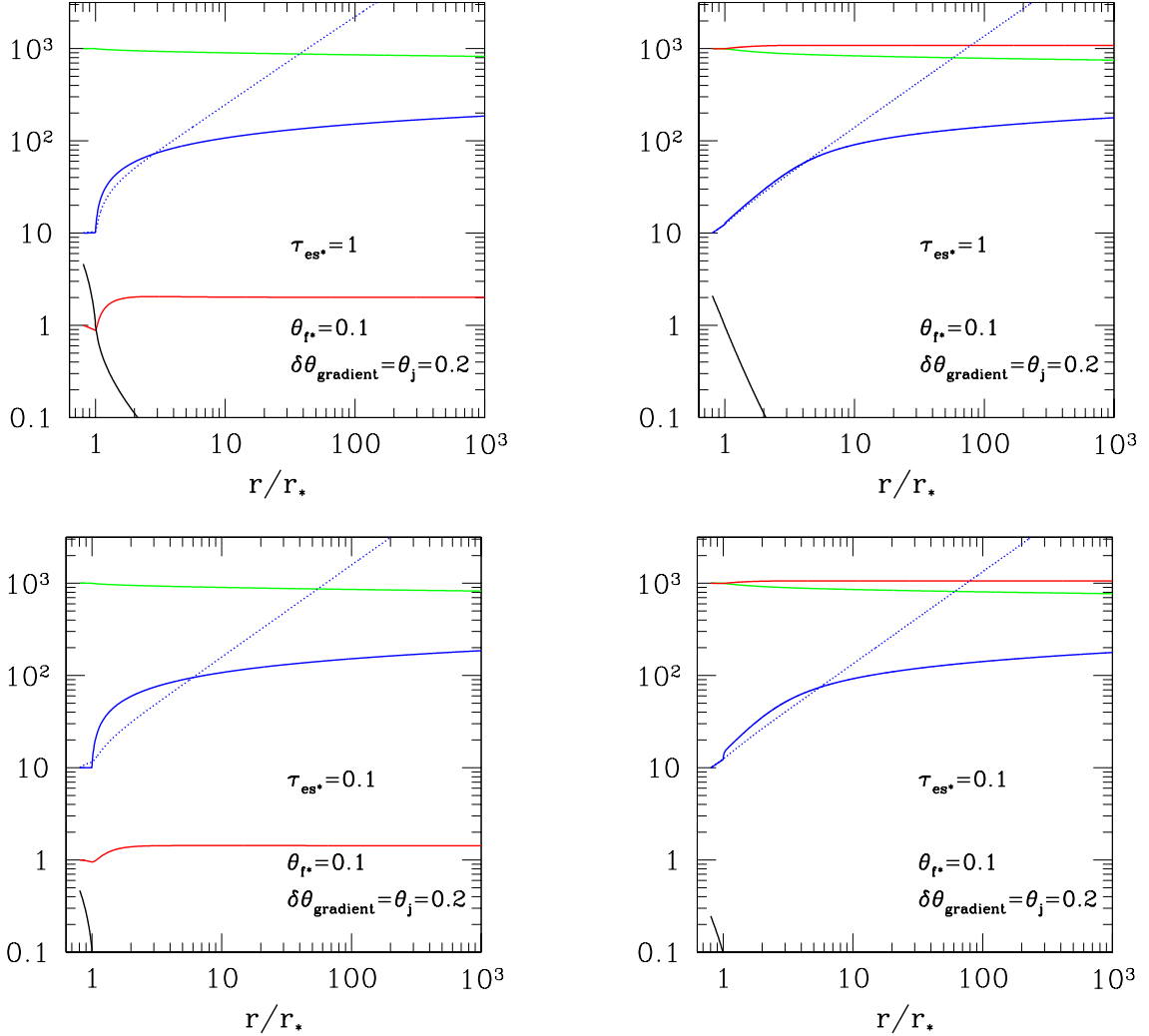


FIG. 4.— Same as Figure 3, but for  $\tau_{\text{es}*} = 1$  (top plots) and  $\tau_{\text{es}*} = 0.1$  (bottom plots).

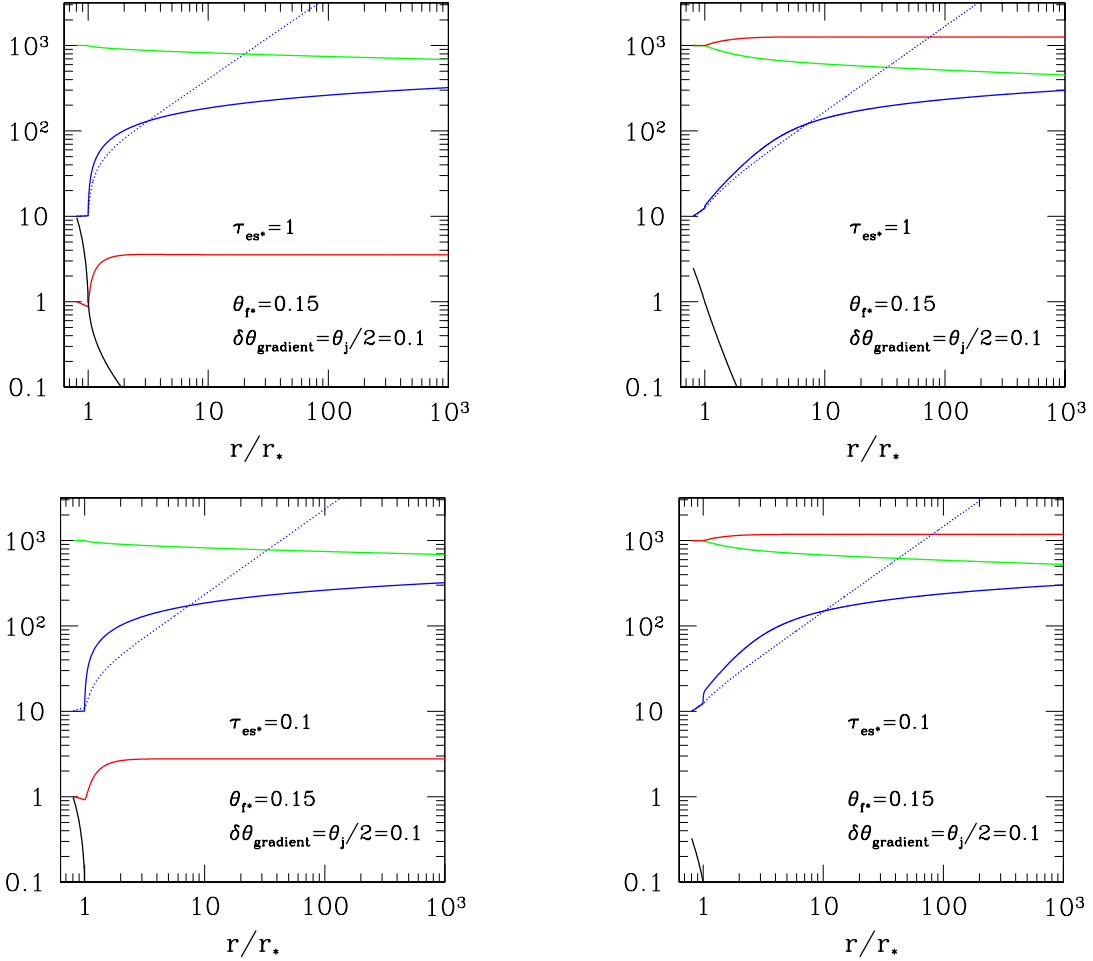


FIG. 5.— Same as Figures 3, 4, except  $\delta\theta_{\text{gradient}} = \theta_j/2 = 0.1$  and  $\theta_{f*} = 0.15$ . Optical depth at breakout:  $\tau_{\text{es}*} = 10$  in top plots and  $\tau_{\text{es}*} = 0.1$  in bottom plots.

and then iterate. The Lorentz force term in  $d\Gamma/dr$  is only valid outside the fast magnetosonic critical point, and so we take  $\Gamma(r_i) \gtrsim \Gamma_c \simeq \sigma_*^{1/3}$ . Radial integrations are done using a 5th-order Runge-Kutta algorithm with adaptive step size (see Sections 7.3, 7.5 of Kiusalaas 2010).

Results are plotted in Figure 3 for an outflow with magnetization  $\sigma_i = \sigma_* = 1000$ , and both low and high radiation fluxes ( $\mathcal{R}_i = 1, 1000$ ) at the inner boundary. The action of the Lorentz force is concentrated at a small radius where the flaring is most severe, causing an increase in  $\Gamma$  that is initially much faster than linear. When the radiation energy flux is weak compared with the magnetic Poynting flux, the outflow experiences strong but logarithmic acceleration after breakout with  $\Gamma \propto \ln^{1/2} x$ , a direct consequence of causally limited flaring,  $\delta\theta_f \sim 1/\Gamma$  [equation (33)]. While the optical depth is large, the photon field is advected with the plasma, remaining nearly isotropic in the comoving frame. Once the optical depth falls below unity the photon field decouples and is free to self-collimate, so that  $\Gamma_{\text{eq}} \propto x$ .

High radiation fluxes ( $\mathcal{R} \sim \sigma$ ) force the flow back to the shallower profile  $\Gamma \simeq \Gamma_{\text{eq}}$ , even while the magnetic flaring grows stronger ( $1/\Gamma$  is larger). The acceleration zone is therefore widened in the radial direction compared with the radiation-free jet.

Quite generally, we find that the terminal Lorentz factor is insensitive to the initial radiation energy flux. The growth in radiation energy flux outside the photosphere is therefore largely compensated by a further reduction in outflow magnetization.

We also consider a low scattering depth at the breakout radius. In this case the matter is only weakly coupled to the radiation field, and the Lorentz factor is forced well above  $\Gamma_{\text{eq}}$  a small distance outside the breakout radius (Figure 4). As in the case of higher optical depths, high radiation fluxes limit the growth of  $\Gamma$  and force it toward  $\Gamma_{\text{eq}}$ . But the mismatch between  $\Gamma$  and  $\Gamma_{\text{eq}}$  remains unless  $\mathcal{R} \gtrsim \sigma$ . Energy is transferred from the magnetic field to the photons, resulting in a significantly modified spectrum (Section 4).

Faster jet flaring, corresponding to a jet edge with  $\delta\theta_{\text{gradient}} = 0.5\theta_j$ , produces faster acceleration and terminal Lorentz factors closer to  $\sigma_*$ , but otherwise qualitatively similar behavior (Figure 5).

A novel effect becomes clear when the compactness is large: the magnetization can show a significant reduction, dropping significantly below  $\mathcal{R}$  and even  $\Gamma$ , and therefore resulting in a *weakly* magnetized outflow. This is caused by the strong radiation drag at small radius, which restricts the growth of  $\Gamma$  which allows for stronger jet flaring.



### 3. FLARING, HOT MAGNETIZED JET: TRANSPARENT FLOW ACROSS THE FAST CRITICAL SURFACE (MODEL II)

The dynamics of the outflow can be calculated more precisely in the optically thin regime, where the radiation field is prescribed at an emitting surface (radius  $r_s$ ) and passively collimates outside that surface. This allows us to study the critical point structure of the flow, at the price of neglecting the effects of multiple scattering. In the spherical case, the emission surface could, if one wanted, be identified with the physical surface of a star. But the model of a passively collimating photon field can also be applied to outflows that are already relativistic at the photosphere, including those with a jet geometry. In this section, we solve the wind equations for a steady, flaring jet which is optically thin but sub-magnetosonic at breakout. In contrast to the model presented in Section 2, here we prescribe the flaring profile in advance.

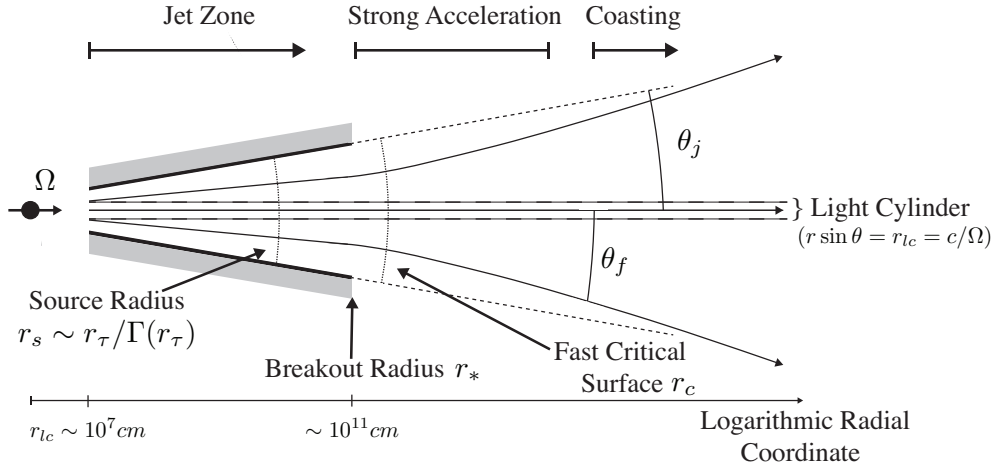


FIG. 6.— Geometry and approximate scale of the flow solutions for jet model II.

The flow geometry is shown in Figure 6. The photon source radius sits in the confined portion of the jet, inside the breakout radius  $r_*$ . After breakout, the optically thin flow is accelerated through the magnetosonic surface, whose location and shape are calculated self-consistently (analytic approximations to the position of the critical surface can be found in Section 3.5). We follow the flow along a field line  $\theta_f(r)$ , situated well outside the light cylinder, from just outside the source radius.

Our solution to the flow below the breakout point formally is in the optically thin regime. Because the jet has already typically attained relativistic motion before breaking out, we can view the photon emission as arising from a virtual surface located below the physical photosphere, at a radius  $r_{s,\text{eff}} \sim r_\tau / \Gamma(r_\tau)$ . At a high radiation intensity, the matter is locked into the bulk frame defined by the photon field,  $\Gamma \simeq \Gamma_{\text{eq}} \sim (r - r_s) / (\theta_j r_s)$ , around breakout. This means that the flow profile closely mimics an optically thick, radiation-dominated flow inside breakout, and we expect that our flow solutions should adequately represent the dynamics of a jet which encounters a photosphere at a radius  $r_* \sim r_\tau > r_s$ .

Our procedure is first to choose the poloidal field geometry and radiation profile, and then evolve the energy and angular momentum along the poloidal flux surfaces. A simple description of the photon field is possible when the jet geometry is locally spherical - that is, when the streamlines are conical inside breakout. This constrains the non-radial Lorentz force to vanish at  $r < r_*$ , which in the small-angle limit can be written as

$$\frac{1}{c} (\mathbf{J} \times \mathbf{B})_\theta \simeq -\frac{B_\phi}{4\pi r \theta} \frac{d(B_\phi \theta)}{d\theta} = 0 \quad \Rightarrow \quad B_\phi \propto \theta^{-1}. \quad (34)$$

A jet with such a line current profile will *de-collimate* at  $r > r_*$ , as the external pressure is removed. This decollimation leads to rapid outward acceleration of the cold matter entrained in the jet, even in the absence of radiative forcing.

Other jet profiles are easily constructed and may be more natural: in the cold MHD jet calculation of Tchekhovskoy et al. (2010), the confining surface has a parabolic structure inside breakout, transitioning to a conical geometry outside. Nonetheless, the radial Lorentz factor profiles that we obtain are (in the absence of radiation) very similar to those of Tchekhovskoy et al. (2010), and only depend on the magnitude of the differential flaring between magnetic flux surfaces.

We focus on the local dynamics within magnetic flux surfaces, taking into account the effect of radiation pressure. This longitudinal dynamics is sensitive to the relative flaring rates of neighboring flux surfaces, but not to the global profile of Poynting flux transverse to the jet axis. Although the transverse force balance is not explicitly taken into account, we do check that i) the degree of magnetic flaring is consistent with causal stresses; and ii) that the transverse component of the radiation force is weak compared with the transverse Lorentz force (so that the radiation flow is not strong enough to comb out the field lines into a conical geometry: see Appendix D).

### 3.1. Jet Properties

To construct an optically thin radiation field, we consider the simplest case of uniform intensity  $I = \int I_\nu d\nu$  at the emission radius  $r_s$ , as we did in Paper I, but now restrict the sampling of the radiation field to polar angles  $\theta < \theta_j$ . The emission patch covers a small angular disk of area  $\pi(\theta_j r_s)^2$  (Figure 6), and the luminosity per sterad is  $dL_{\gamma^*}/d\Omega \sim \pi\theta_j^2 I$ . This allows an analytic calculation of the radiation force acting on a particle of arbitrary Lorentz factor and direction, which is presented in Appendix A. This result generalizes the simpler angular momentum formalism used in Section 2 and presented in equation (24).

We showed in Paper I that if we normalize the photon intensity and the angular width of the photon beam by fixing i) the radiation force and ii) the relativistic frame  $\Gamma_{\text{eq}}$  in which this force vanishes, then other quantities, such as the mean power radiated by an electron in its bulk frame, are nearly identical to those obtained from a radiation field that is isotropic at a relativistically moving photosphere.

The radiation streams freely outward at  $r > r_s$ , and its cone contracts with increasing radius. The size and orientation of this cone now vary with distance from the jet axis (in contrast with the case of a spherical emission surface; Paper I). There is generally a misalignment of the direction of peak radiation intensity with respect to both the radial direction, and the local flow direction. The alignment is strongest at a small but finite distance from the rotation axis, and produces a peak in the radiation force there.<sup>1</sup>

We normalize distances to  $r_s$ , but measure the photon compactness (11) at the breakout radius,

$$x \equiv \frac{r}{r_s}; \quad \omega \equiv \frac{\Omega_f r_s}{c}; \quad \chi_* \equiv \frac{\sigma_T r_* \pi \theta_j^2 I}{\dot{m} c^3 (x_* - 1)^2}. \quad (35)$$

In a GRB outflow, the photosphere generally lies outside the light cylinder of the rotating engine, so we take  $\omega = \Omega_f r_s / c > 1$  in our calculations. In this context, the magnetization can be most simply defined as<sup>2</sup>

$$\sigma \equiv \frac{B_r^2 \Omega_f^2 (r \theta_f)^2}{4\pi \Gamma \rho v_r c^3} \quad (\theta_f \ll 1). \quad (36)$$

Neglecting the radiation field, the energy and angular momentum per unit rest mass are given by

$$\mu c^2 = \left( \Gamma - \Omega_f \frac{B_r B_\phi}{4\pi \Gamma \rho v_r} \right) c^2; \quad \mathcal{L} r_s c = \left( \Gamma v_\phi - \frac{B_r B_\phi}{4\pi \Gamma \rho v_r} \right) r \theta_f, \quad (37)$$

and in a steady MHD outflow are conserved along field lines. They can be written in a dimensionless form,

$$\mu = \Gamma - \frac{\sigma}{\omega x \theta_f} \frac{B_\phi}{B_r} \simeq \Gamma + \sigma; \quad \mathcal{L} = \Gamma x \theta_f \beta_\phi - \frac{\sigma}{\omega^2 x \theta_f} \frac{B_\phi}{B_r} \equiv \mathcal{L}_m + \mathcal{L}_p. \quad (38)$$

### 3.2. Poloidal Field Configuration

To incorporate a strong radial Lorentz force into the outflow, we choose the poloidal flux surfaces by fixing the function  $\theta_f(x, \theta_{f*})$ , where  $\theta_{f*}$  is the polar angle at the breakout radius. The Lorentz force is large and positive if neighboring flux surfaces diverge from each other more rapidly than in a monopolar geometry. The effect of this differential expansion appears in the wind equations via the function

$$A(x, \theta_{f*}) \equiv \frac{d \ln \theta_f}{d \ln \theta_{f*}}; \quad B_r = \frac{B_{r*} x_*^2}{A x^2} \left( \frac{\theta_{f*}}{\theta_f} \right)^2; \quad \sigma = \frac{\sigma_*}{A}. \quad (39)$$

We focus on the dynamics along a single flux surface, and so do not have to consider the angular dependence of  $B_{r*} = B_r(r_*)$ . The critical point structure of the longitudinal flow is insensitive to angular gradients in the flow magnetization.

The flaring profile used in our calculations is described in Section 3.4, followed by the numerical results.

### 3.3. Longitudinal Wind Equations

We now consider the longitudinal evolution of the outflow variables along a magnetic flux surface. A radiation force (20) is added to the Euler equation, which becomes

$$\rho \Gamma \mathbf{v} \cdot \nabla (\Gamma \mathbf{v}) = \frac{1}{4\pi} [(\nabla \cdot \mathbf{E}) \mathbf{E} + (\nabla \times \mathbf{B}) \times \mathbf{B}] + \frac{\Gamma \rho}{m} \mathbf{F}^{\text{rad}}. \quad (40)$$

<sup>1</sup> A tiny portion of the outer jet sits inside the light cylinder of the engine, and formally retains strong rotation of its field lines, which reduces the overlap between the radiation and fluid flows. This effect will, in practice, probably be eliminated by turbulence in the jet.

<sup>2</sup> This definition, following Michel (1969) and Goldreich & Julian (1970), differs in terms  $O(v_\phi / \Omega_f r \sin \theta_f)$  to  $\sigma = (c^2 d\dot{M} / d\Omega)^{-1} dL_p / d\Omega$ , the definition used in Section 2; and to  $\sigma = (c^3 d\dot{M} / d\Omega)^{-1} \dot{\Phi}_\phi^2$ , where  $\dot{\Phi}_\phi = v_{r,r} \sin \theta_f B_\phi$  is the advection rate of toroidal flux. We use equation (36) is independent of radius if the poloidal field is restricted to be purely radial, but the last two definitions are non-constant at  $O(v_\phi / \Omega_f r \sin \theta_f)$ .

Taking the dot product of equation (40) with the unit poloidal field vector  $\hat{B}_p$ , defining the longitudinal derivative  $\partial_l = \hat{B}_p \cdot \nabla$ , and taking the small-angle limit, we have

$$\partial_l \Gamma c^2 - \frac{v_\phi}{r\theta_f} \partial_l \mathcal{L}_m = -\frac{B_\phi}{4\pi\Gamma\rho r\theta_f} \partial_l (r\theta_f B_\phi) + \frac{F_p^{\text{rad}}}{\bar{m}} \quad (41)$$

The  $\phi$ -component of equation (40) is

$$v_p \partial_l \mathcal{L}_m = \frac{B_p}{4\pi\Gamma\rho} \partial_l (r\theta_f B_\phi) + (r\theta_f) \frac{F_\phi^{\text{rad}}}{\bar{m}}. \quad (42)$$

Here  $\mathcal{L}_m$  is the specific matter angular momentum [equation (38)], and we have made use of the fact that the poloidal flow velocity  $\mathbf{v}_p$  is aligned with  $\mathbf{B}_p$ . The Coulomb force only contributes to the transverse force balance and does not appear in equations (41) or (42). Both of these features are easily derived by noting that the toroidal electric field vanishes in a steady, axisymmetric MHD wind ( $\mathbf{E} \cdot \mathbf{B} = 0$ ), which implies that  $\mathbf{v}_p \times \mathbf{B}_p = 0$  and  $\mathbf{E}_p \cdot \mathbf{B}_p = 0$ .

In Appendix A we calculate the radiation force (20) in a thin jet, and express the poloidal and toroidal components in terms of dimensionless functions  $R_j, P_j$ ,

$$F_p^{\text{rad}} = \chi_* \frac{\bar{m}c^2}{r_s} R_j(r, \Gamma, \beta_\phi); \quad F_\phi^{\text{rad}} = \chi_* \frac{\bar{m}c^2}{r_s} P_j(r, \Gamma, \beta_\phi). \quad (43)$$

Rotation of the photon field at the emission surface tends to reduce the azimuthal drag. It can be incorporated by modifying the  $\beta_\phi$ -dependence of equations (43), as is discussed in Appendix B, but is generally negligible when the outflow lies far outside the light cylinder ( $\omega \gg 1$ ).

A good approximation to the poloidal force can be obtained on field lines  $(x\omega)^{-1} \ll \theta_f \ll \theta_j$ ,

$$R_j \simeq \frac{x_*}{4x^2\Gamma^2} \left( 1 - \frac{\theta_j^4 \Gamma^4}{3x^4} \right), \quad (44)$$

in agreement with equation (24). The result for a spherical emission surface (Paper I) differs only in the absence of the factor  $\theta_j^4$ . The vanishing of the radiation force occurs at a significantly higher Lorentz factor when the photon beam is collimated,

$$\Gamma_{\text{eq}} \simeq \frac{x-1}{\theta_j} \quad (45)$$

up to a numerical factor of order unity as shown in Figure 15.

The deviation of the field lines from a purely radial direction is measured by  $\Delta\theta_B = B_\theta/B_r$ , which we take to be small, so that  $B_p = (1 + \Delta\theta_B^2)^{1/2} B_r \simeq B_r$ ,  $v_p \simeq v_r$ . As is detailed in Appendix C, the derivatives along field lines on the right hand side of equations (41) and (42) can be written in the small-angle approximation. Ignoring the cross-field force balance then allows us to express (41), (42) as two ordinary differential equations, which can be re-written in terms of  $d\Gamma/dl$  and  $d\mathcal{L}_m/dl$ . The various terms on the right-hand side of these equations can be separated into purely magnetocentrifugal pieces (which do not depend on the radiation force), the direct radiation force, and a cross term:

$$\frac{d\Gamma}{dl} = \frac{\Gamma'_\sigma + \Gamma'_{\sigma\chi} + \Gamma'_\chi}{\mu_{\text{eff}}}; \quad \frac{d\mathcal{L}_m}{dl} = \frac{(\mathcal{L}'_m)_\sigma + (\mathcal{L}'_m)_{\sigma\chi} + (\mathcal{L}'_m)_\chi}{\mu_{\text{eff}}} \quad (46)$$

where

$$\Gamma'_\sigma + \Gamma'_{\sigma\chi} + \Gamma'_\chi \equiv -\frac{\sigma}{x\theta_f\omega\beta_r} \Psi - \frac{\sigma\chi_*}{(x\theta_f\omega)^2\beta_r\Gamma} \left( R_j + \frac{B_\phi}{B_r} P_j \right) \Lambda + \chi_* \left( R_j + \frac{\beta_\phi}{\beta_r} P_j \right) \quad (47)$$

$$(\mathcal{L}'_m)_\sigma + (\mathcal{L}'_m)_{\sigma\chi} + (\mathcal{L}'_m)_\chi \equiv -\frac{\sigma}{x\theta_f\omega^2\beta_r} \Psi - \frac{\sigma\chi_*}{x\theta_f\omega^2\beta_r\Gamma} \left( \beta_\phi \Lambda + \frac{1}{\beta_r\Gamma^2} \frac{B_\phi}{B_r} \right) \left( R_j + \frac{B_\phi}{B_r} P_j \right) + \chi_* \frac{x\theta_f}{\beta_r} P_j \quad (48)$$

where

$$\Lambda \equiv 1 + \frac{\beta_\phi}{\beta_r} \frac{B_\phi}{B_r}; \quad \Psi \equiv \left( 1 + \frac{\Delta\theta_B}{\theta_f} \right) (1 + \Lambda) \frac{\beta_\phi}{x} + \frac{B_\phi}{B_r} \frac{\beta_r}{A} \frac{dA}{dl} \quad (49)$$

and

$$\mu_{\text{eff}} \equiv 1 - \frac{\sigma}{(\beta_r\Gamma)^3} (1 + \beta_\phi^2\Gamma^2) - \frac{\sigma}{(x\theta_f\omega)^2\beta_r\Gamma} \left( 1 + \frac{\beta_\phi^2}{\beta_r^2} \right) + \frac{2\sigma\beta_\phi}{x\omega\theta_f\beta_r^3\Gamma} \quad (50)$$

is the effective inertia.

### 3.4. Poloidal Field Profile

We now prescribe the poloidal field profile outside the breakout surface, which, in a steady jet, also determines the poloidal streamlines. The profile inside  $r_*$  is assumed to be straight and conical,  $\theta_{f*} = \theta_{f,s}$ . A strong Lorentz force is obtained outside  $r_*$  if the net change  $\theta_{f,\infty} - \theta_{f*}$  in polar angle is itself a growing function of  $\theta_{f*}$ . A simple choice, that is asymptotically conical at a large radius, is

$$\frac{\theta_f(x)}{\theta_{f*}} = 1 + \frac{\theta_{f*}}{\delta\theta} \left(1 - \frac{x_*}{x}\right)^\alpha \quad (x > x_*). \quad (51)$$

This connects smoothly with the inner cone if  $\alpha > 1$ . The net change in polar angle is determined by<sup>3</sup>  $\delta\theta$ ,

$$\theta_{f,\infty} - \theta_{f*} = \left(\frac{\theta_{f*}}{\delta\theta}\right) \theta_{f*}. \quad (52)$$

The local change in the field line direction, relative to the total bend, is

$$\frac{\Delta\theta_B}{\theta_f - \theta_{f*}} = \frac{B_\theta/B_r}{\theta_f - \theta_{f*}} = \frac{2\alpha x_*}{x - x_*}. \quad (53)$$

The flux spreading factor works out to  $A = 2 - \theta_{f*}/\theta_f$  for any field-line profile of the form (51). In the absence of radiation, the Lorentz factor can be obtained by imposing energy conservation. It depends on the flaring profile of the jet via

$$\begin{aligned} \Gamma &\simeq \Gamma_* + \sigma_* - \sigma = \Gamma_* + \sigma_* (1 - A^{-1}) = \Gamma_* + \sigma_* \frac{\theta_f/\theta_{f*} - 1}{2\theta_f/\theta_{f*} - 1}; \\ \Gamma_\infty &\simeq \Gamma_* + \sigma_* \frac{\theta_{f*}/\delta\theta}{1 + 2\theta_{f*}/\delta\theta}. \end{aligned} \quad (54)$$

The acceleration tends to be more concentrated in radius for smaller values of the parameter  $\alpha$ ; in what follows  $\alpha = 2$ . In Figure 7 we show sample field lines given by (51) with strong flaring ( $\delta\theta = 0.3$ ) for several values of  $\theta_{f*}$ .

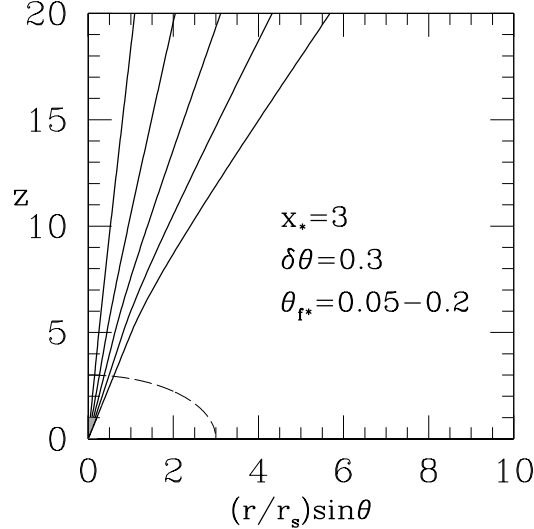


FIG. 7.— Sample field line profiles of the type (51) with strong flaring ( $\delta\theta = 0.3$ ) and breakout radius  $x_* = r_*/r_s = 3$  (dashed line). The emission radius bounds the inner grey zone.

### 3.5. Position of Fast Magnetosonic Surface

When the flow speed surpasses the fast magnetosonic speed, radial magnetic disturbances are swept downstream and cannot interact with the part of the jet interior to the fast critical surface. The inertia of the electromagnetic field also becomes insignificant in the radial force balance, so that radiation pressure is relatively more important. We first consider how the position  $x_c = r_c/r_s$  of the critical surface is modified by field-line flaring, and then consider the effects of radiation. The critical surface sits at infinite radius only if the poloidal magnetic field is constrained to be radial and radiation is absent (Goldreich & Julian 1970).

The critical surface is obtained by setting  $\mu_{\text{eff}} = 0$  in equations (46). Retaining  $\chi_* = 0$ , and assuming  $\sigma \gg 1$ , this corresponds to  $\Gamma \simeq \sigma^{1/3}$  [a vanishing coefficient of  $d\Gamma/dl$  in equation (C4)], and  $\Psi = 0$ . When  $\delta\theta_f = O(\theta_j)$ , the magnetofluid rapidly accelerates

<sup>3</sup> This is the analog of the parameter  $\delta\theta_{\text{gradient}}$  appearing in jet Model I, used to approximate the derivative in equation (33).

outside radius  $r_*$ , and so we can expand  $A \simeq 1$  near this radius:

$$\frac{dA}{d \ln l} \simeq \alpha \frac{\theta_{f*}}{\delta \theta} \left(1 - \frac{x_*}{x}\right)^{\alpha-1} \frac{x_*}{x}; \quad \Psi \simeq \frac{1}{x^2 \theta_f \omega} - (x \theta_f \omega) \frac{dA}{dt}. \quad (55)$$

Here we have approximated  $\beta_\phi \simeq 1/x\theta_f\omega \ll 1$ . Then, for  $\alpha = 2$ ,

$$\frac{x_c}{x_*} \simeq 1 + \frac{\delta \theta / \theta_{f*}}{2(x_* \theta_{f*} \omega)^2}. \quad (56)$$

In the absence of magnetic-field flaring, the radiation stress forces the fast surface in from infinity (Paper I). Taking instead  $\delta \theta = \infty$  but allowing for finite  $\chi_*$ , the fast surface corresponds to  $\Gamma \simeq \sigma^{1/3}$  and  $\Gamma'_\sigma \simeq \Gamma'_\chi$ . Then

$$\frac{x_c}{x_*} \simeq \frac{4\sigma^{5/3}}{\chi_* (x_* - 1)^2 \omega^2 \theta_{f*}^2}. \quad (57)$$

This differs from the spherical case (Paper I) mainly by the factor  $1/\theta_{f*}^2$ . At a very high compactness, the flow is tied to the collimating radiation field, and thus the critical surface is pulled in to where  $\Gamma_{\text{eq}}(x, \theta_f) \simeq \Gamma_c \simeq \sigma^{1/3}$ .

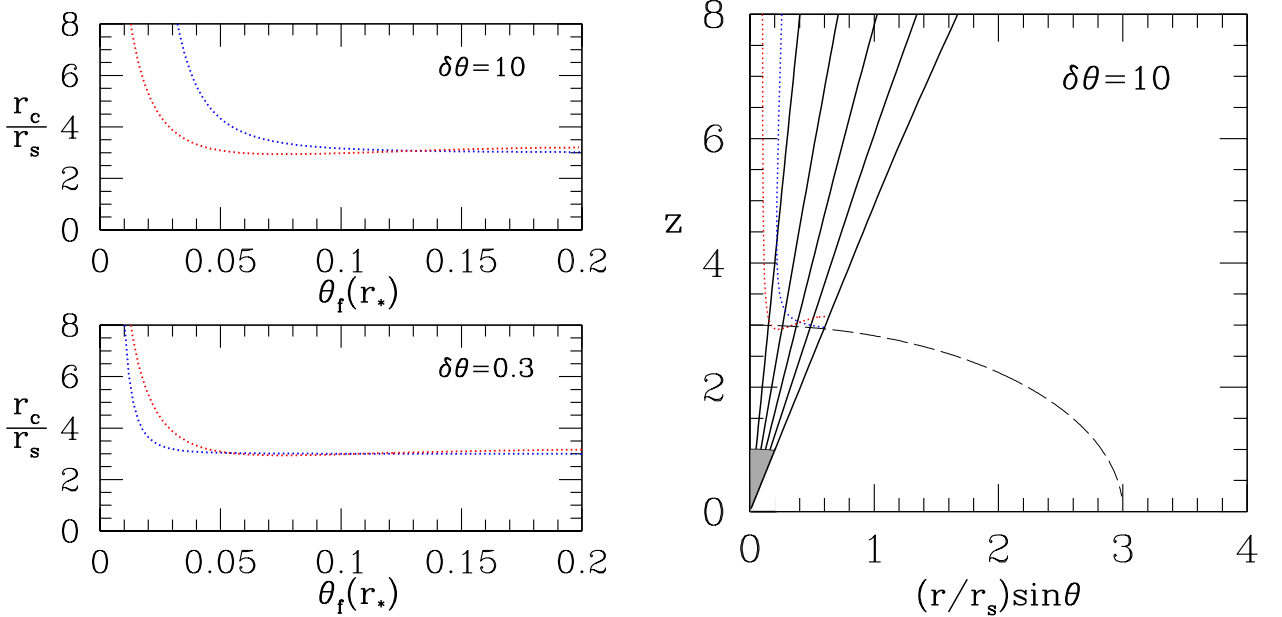


FIG. 8.— Magnetosonic surface inside a flaring jet at low radiation compactness (dotted blue,  $\chi \rightarrow 0$ ) and high compactness [dotted red,  $\chi/\sigma \ll 1$  but still satisfying the bound given in equation (D3)]. *Left panels:* Radius  $x_c = r_c/r_s$  of the magnetosonic point as a function of field line footprint angle, for weak flaring (top) and strong flaring (bottom). *Right panel:* Two dimensional depiction of the magnetosonic surface (weak flaring).

The fast surface is shown as a function of angle in Figure 8, for a breakout radius  $x_* = 3$ . At low radiation compactness, this surface typically lies just outside breakout,  $x_c \gtrsim x_*$ , in agreement with equation (56). As the compactness is increased, the critical surface can either move inward or outward, depending on the location where  $\Gamma_{\text{eq}} = \sigma^{1/3}$ . The critical surface is typically pulled inward near the rotation axis if the magnetic field is weakly flared, and also at larger polar angles if  $x_* \gg \theta_j \sigma^{1/3}$ . Then its position follows equation (57) until reaching the high-compactness limit at

$$\chi_* \simeq \frac{4\sigma^{4/3}}{x_* \omega^2 \theta_{f*}^2 \theta_j}. \quad (58)$$

If alternatively the breakout radius is small, then the critical surface is pushed out by radiation drag,

$$\frac{x_c}{x_*} \simeq \left( \frac{\chi_*}{24\sigma^{1/3}} \frac{\delta \theta}{\theta_{f*}} \frac{\theta_j^4}{x_*^4} \right)^{1/7}, \quad (59)$$

reaching its high-compactness limit at

$$\chi_* \simeq 24 \frac{\theta_{f*}}{\delta \theta} \left( \frac{\theta_j}{x_j} \right)^3 \sigma^{8/3}. \quad (60)$$

The deviation of  $x_c$  toward large radius that is seen close to the rotation axis is due to a combination of effects: a reduction in the outward Lorentz force due to the weaker field-line flaring; and a mis-match between the radiation and matter flows driven by strong rotation. The first effect dominates at low  $\chi_*$ . The change in critical radius at high  $\chi_*$  can be estimated using equation (A17) for  $\Gamma_{\text{eq}}$  near the axis:

$$x_c \simeq \frac{\sigma^{1/3}}{\omega\theta_f}, \quad (\theta_f \ll \omega^{-1}\theta_j^{-1}). \quad (61)$$

### 3.6. Numerical Results

We now examine the solutions to the wind equations (46)-(50) that we have derived for a geometrically and optically thin jet. The singularity at the fast magnetosonic critical point, and the stiffness of the equations associated with large values of  $\sigma$  and  $\chi$ , means that simple integration techniques such as Runge-Kutta are inadequate. To determine the position of the critical point and the flow solution inside it, we use the relaxation method described in Paper I (see also London & Flannery 1982).

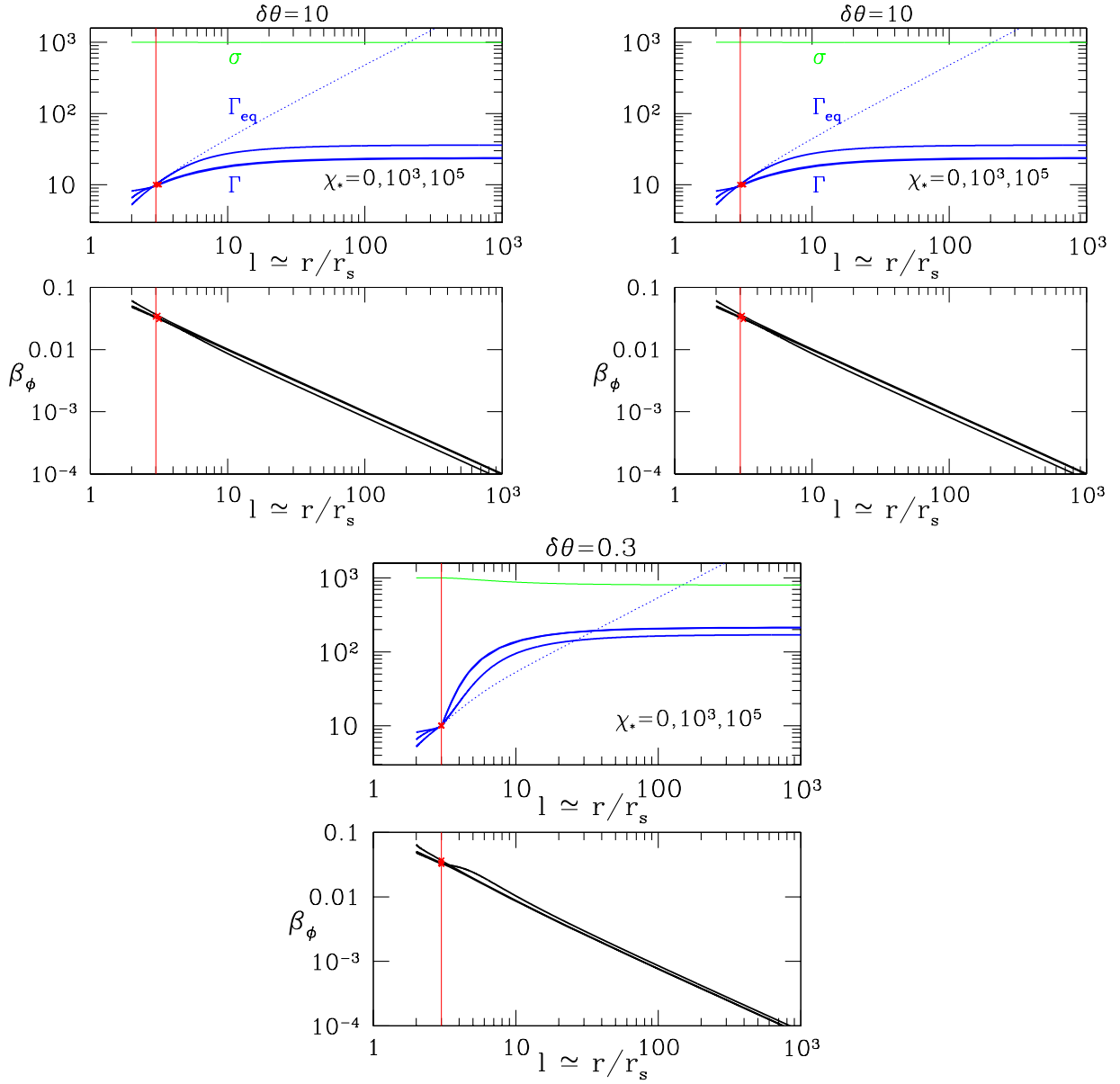


FIG. 9.— Acceleration in a thin, strongly magnetized jet ( $\sigma_* = 1000$ ,  $\omega = 100$ ,  $\theta_j = 0.2$ ), along a field line anchored at  $\theta_{f*} = 0.1$ . The radiation compactness at the breakout radius  $x_* = r_*/r_s = 3$  is varied:  $\chi_* = 1, 10^3, 10^5$ , corresponding to the top to bottom curves on the left side. *Left panel:*  $\delta\theta = 10$  (weak flaring); *right panel:*  $\delta\theta = 1$ ; *bottom panel:*  $\delta\theta = 0.3$  (strong flaring). (The distance along the field line  $l$  differs little from the radial coordinate since the degree of flaring is small).

The inner boundary radius  $r_i$  of the integration is chosen somewhat differently than in Paper I: we set it to twice the photon emission radius ( $x_i = 2$ ) because we only evaluate the radiation force where photons propagate at small angles with respect to the jet axis (requiring that  $x_i - 1 \gg \theta_j$ ). The solutions for  $\Gamma$  and  $\mathcal{L}_m$  obtained by an integration inside the critical point are required to be smooth near  $x_i$ ; avoiding sharp gradients restricts the boundary values at  $x_i$  to a narrow range. We also make a first guess for the critical point radius  $x_c$ . The regularity of the solution at  $x_c$  then allows us to determine the flow variables at the critical point from the equations

$$(\Gamma'_\sigma + \Gamma'_{\sigma\chi} + \Gamma'_\chi)_{x_c} = 0 = \mu_{\text{eff}}(x_c). \quad (62)$$

An approximate solution is chosen which connects the inner boundary values to the critical point.<sup>4</sup> This solution, along with the position of the critical point, is then relaxed to within a desired tolerance using a Newton-Raphson method, all the while satisfying the regularity condition (62). As a last step, the flow outside the critical point is obtained by shooting outward using a fifth-order Runge-Kutta algorithm.

Solutions are obtained for a range of photon compactness and a high magnetization ( $\sigma_* = 1000$ ). The part of the jet studied sits well outside the light cylinder,  $\omega = 100$  in equation (35). Choosing the flaring profile (51), we follow the flow along a field line with initial footprint  $\theta_{f*} = 0.1$ , in a jet of half-opening angle  $\theta_j = 0.2$  and a breakout radius  $x_* = 3 = 1.5x_i$ . The magnitude of the jet flaring is adjusted by choosing the parameter  $\delta\theta$ , with values 10, 1, 0.3 corresponding to a net angular shift  $\theta_{f,\infty}/\theta_{f*} - 1 = 0.1\theta_{f*}, \theta_{f*}, 3.3\theta_{f*}$  between breakout and infinity. The maximal flaring chosen ( $\delta\theta = 0.3$ ) still satisfies equation (17), and so the divergence of neighboring magnetic field lines is consistent with causal stresses.

The results are shown in Figure 9. At low radiation compactness, they resemble those obtained by Tchekhovskoy et al. (2010) for a cold MHD jet. A slow, nearly linear, increase in  $\Gamma$  within the star is followed by rapid (but logarithmic) growth beyond the breakout point, where the field lines begin to diverge. As  $\chi_*$  increases above  $\sim \sigma$ , photon drag begins to dominate the weak Lorentz force inside the breakout radius, and  $\Gamma$  tends to  $\Gamma_{\text{eq}} \simeq x/\theta_j$  [equation (45)]. After breaking out, the fluid is quickly accelerated through the fast point. A strong radiation field forces the position of the critical point to a radius where  $\Gamma_{\text{eq}} \simeq \sigma_*^{1/3}$  (in this case, the displacement is outward). We do not search for solutions with the fast point inside the star, corresponding to  $x_* \gtrsim 3$ .

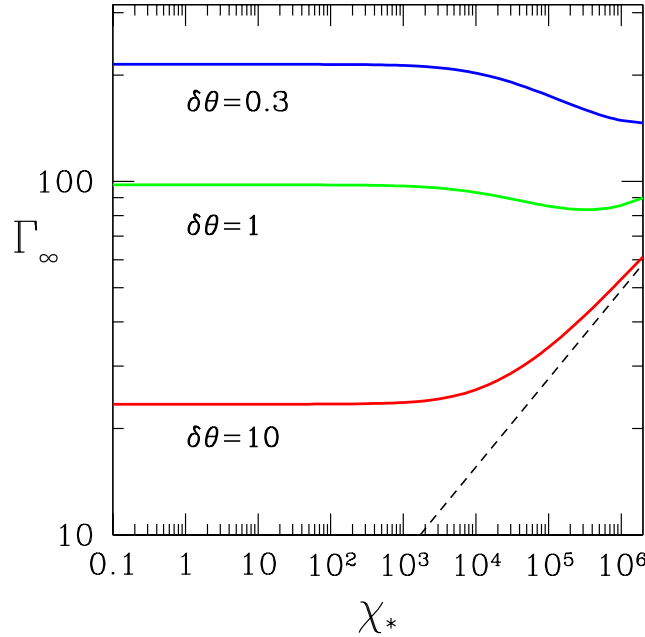


FIG. 10.— Asymptotic Lorentz factor of flaring magnetized jet ( $\sigma_* = 1000$ ,  $\omega = 100$ ,  $\theta_j = 0.2$ ), as a function of compactness  $\chi_*$  at the breakout radius. Curves correspond to a field line anchored at  $\theta_{f*} = 0.1$  and represent varying degrees of flaring (weak:  $\delta\theta = 10$ ; intermediate:  $\delta\theta = 1$ ; strong:  $\delta\theta = 0.3$ ). Dashed black line: asymptotic Lorentz factor  $0.8(\chi_* x_* / 4\theta_j)^{1/4}$  of an unmagnetized, radial, monopolar outflow.

The influence of the radiation field can be clearly seen in the dependence of asymptotic Lorentz factor  $\Gamma_\infty$  on  $\chi_*$  (Figure 10). When flaring is strong ( $\delta\theta \lesssim 1$ ), the matter is pushed rapidly to  $\Gamma > \Gamma_{\text{eq}}$  and it feels a net drag outside the magnetosonic point. The asymptotic Lorentz factor is reduced from (54). At very high  $\chi_*$ , the radiation drag is able to suppress the acceleration and, therefore, the asymptotic Lorentz factor.

The minimal compactness needed to significantly affect the post-breakout flow can be estimated by equating the leading terms

<sup>4</sup> This procedure is followed for a discrete set of values of  $\chi_*$ , after which the inner boundary condition on  $\Gamma$ ,  $\mathcal{L}_m$  is chosen from an interpolating function.

in (47) at  $x = 3x_*/2$ , the point where the relative flaring of poloidal field lines is maximal. This gives

$$\chi_* \gtrsim \sigma_*^{5/3} \frac{\theta_{f*}}{\delta\theta}. \quad (63)$$

In this case, the sign of the effect of radiation pressure outside the critical point still depends on the degree of magnetic field line flaring. If flaring is weaker ( $\delta\theta \gtrsim 1$ ) then the details of the flow profile near breakout differ from the unmagnetized flow, but  $\Gamma_\infty$  is still well approximated by an unmagnetized, radiatively driven flow:

$$\Gamma_\infty \simeq 0.8(\chi_* x_*/\theta_j)^{1/4} \quad (\sigma = 0, \delta\theta \rightarrow \infty). \quad (64)$$

Our solutions, in the part of parameter space that we have explored, satisfy two basic constraints. First, the outflow is optically thin at (or near) breakout if the compactness sits below the bound (15). Second, the component of the radiation force transverse to the poloidal flux surfaces must remain small compared with the transverse Lorentz force that is implied by the chosen flaring profile. The corresponding upper bound (D3) on the compactness is derived in Appendix D.

#### 4. SPECTRUM OF SCATTERED PHOTONS

We now consider the self-consistent spectrum of photons that scatter off a hot electromagnetic outflow near its photosphere. Our focus is solely on the signature of the differential flow of matter and photons – that is, we neglect any internal processes that would heat particles or induce small-scale deviations from a uniform flow.

We first consider the jet model of Section 2, in which the optical depth is finite but the flow is considered only outside its fast magnetosonic surface. Then we turn to the optically thin jet model of Sections 3 and 3.6, in which the entire flow is solved inside and outside the critical surface, but the region interior to the photosphere is ignored. As in Paper I, we neglect any internal dissipation in the outflow, which can contribute to the high-energy tail of the spectrum (Thompson 1994; Giannios 2006; Beloborodov 2010).

##### 4.1. Spectrum in Jet Model I (Super-magnetosonic): Monte Carlo Method

Here we follow the photon field self-consistently across the jet photosphere, which is assumed to sit outside the fast magnetosonic point (Figure 1). The exchange of energy between photons and magnetic field was calculated in Section 2 in parallel with the flaring rate of the poloidal field lines outside a fixed breakout radius. The radiation force on the matter, and the evolution of the equilibrium Lorentz factor  $\Gamma_{\text{eq}}$  of the radiation field, defined in equations (23) and (24), are both calculated by taking angular moments (21) of the intensity.

To calculate the emergent spectrum, we i) take the flow velocity profile as a given background, and then ii) inject photons from the inner radius  $r_i = 0.8r_*$  with an isotropic distribution in a frame moving with Lorentz factor  $\Gamma_{\text{eq},i}$ . Photon parameters in the rest frame of the ‘star’ at  $r > r_i$  are obtained by a simple Lorentz boost. Defining a radial direction cosine by  $\mu = \hat{k} \cdot \hat{r}$ , one has  $\mu = (\mu' + \beta)/(1 + \beta\mu')$ ,  $\omega = \Gamma(1 + \beta\mu')\omega'$ , where the prime labels the matter rest frame. Deviations from radial flow are assumed small compared with the width of the photon beam.

Electron scatterings are handled in the Thomson approximation (the outflow moves relativistically in the case of a GRB), by drawing a random number  $1 - e^{-\Delta\tau_{\text{es}}}$ . The position of the next scatter point is calculated by integrating

$$\Delta\tau_{\text{es}}[r_1, r_2, \mu(r_1)] = \alpha_{\text{es}*} r_* \int_{r_1}^{r_2} [1 - \mu(r)\beta(r)] \frac{r_* dr}{\mu(r)\beta(r)r^2} \quad (65)$$

along the photon ray. Note that the outflow solution of Section 2 has been iterated so that the coefficient  $\alpha_{\text{es}*}$  corresponds to a prescribed value of the radial optical depth  $\tau_{\text{es}}(r_*, \infty, 1)$  at the breakout radius. Other initial flow parameters are defined at  $r_i$ . The direction cosine evolves from a scattering radius  $r$  to  $r_2 > r$  according to

$$1 - \mu(r_2)^2 = \left(\frac{r}{r_2}\right)^2 [1 - \mu(r)^2] \quad (r_2 > r). \quad (66)$$

The photon escapes if  $\Delta\tau_{\text{es}}$  exceeds the total optical depth along the ray.

The frequency distribution of the outgoing photons is first obtained with a monochromatic photon source,  $I_\nu = I_0\nu_0\delta(\nu - \nu_0)$ . This output spectrum is then convolved a source spectrum that is either a pure blackbody, or a function<sup>5</sup> that mimics the low-frequency slope of a GRB,  $F_\nu = \text{const} \times e^{-h\nu/kT_0}$ . For both types of seed spectrum, the temperature  $T_0$  is normalized by requiring  $F_\nu$  to peak at the fixed reference frequency  $\nu_0$ .

Scatterings are taken to be elastic in the bulk frame, where the matter is assumed cold, so that the outgoing and ingoing frequencies satisfy the usual Doppler relation,

$$\frac{\nu_{\text{em}}}{\nu} = \frac{1 - \beta\mu}{1 - \beta\mu_{\text{em}}} = \frac{1 + \beta\mu'_{\text{em}}}{1 + \beta\mu'}. \quad (67)$$

After transforming  $\mu$  to the local bulk frame, we pick scattering angles  $\theta'_s, \phi'_s$  with respect to the flow direction. The direction cosine of the outgoing photon is determined via  $\mu'_{\text{em}} = \mu' \cos\theta'_s + (1 - \mu'^2)^{1/2} \sin\theta'_s \cos\phi'_s$ , followed by a boost to the stellar frame.

<sup>5</sup> This corresponds to the lower-frequency half of the Band function (Band et al. 1993), extended to all frequencies.



The peak of the seed photon distribution is stretched to higher frequencies when the outflow Lorentz factor  $\Gamma \gtrsim \Gamma_{\text{eq}}$  [equation (45)]. A scattered photon has a frequency in the range  $\nu_{\text{min}} < \nu < \nu_{\text{max}}$ , where

$$\nu_{\text{max}} = \frac{1 - \beta \mu_{\text{min}}}{1 - \beta} \nu_0 \simeq \left(1 + \frac{\Gamma^2}{x^2}\right) \nu_0 \quad (x, \Gamma \gg 1) \quad (68)$$

and  $\nu_{\text{min}} = [(1 - \beta)/(1 + \beta)]\nu_0 \sim \nu_0/4\Gamma^2$ .

#### 4.2. Spectrum in Jet Model I: Results

Figure 11 shows spectra for the case where matter and radiation field are initially locked together at  $\Gamma_i = \Gamma_{\text{eq},i} = 10$ . The curves correspond to a variety of optical depths, as well as low and high initial photon fluxes,  $\mathcal{R}_i = 1, 10^3$ . The peak of the spectrum is somewhat broadened compared with a pure blackbody, and the segment shortward in frequency of the peak has a flattened spectrum, although not as flat as is seen in GRBs. A similar effect was seen in Paper I in the case of hot electromagnetic outflows accelerating along a radial, monopolar magnetic field. The spectrum below the peak is flattened even more if the

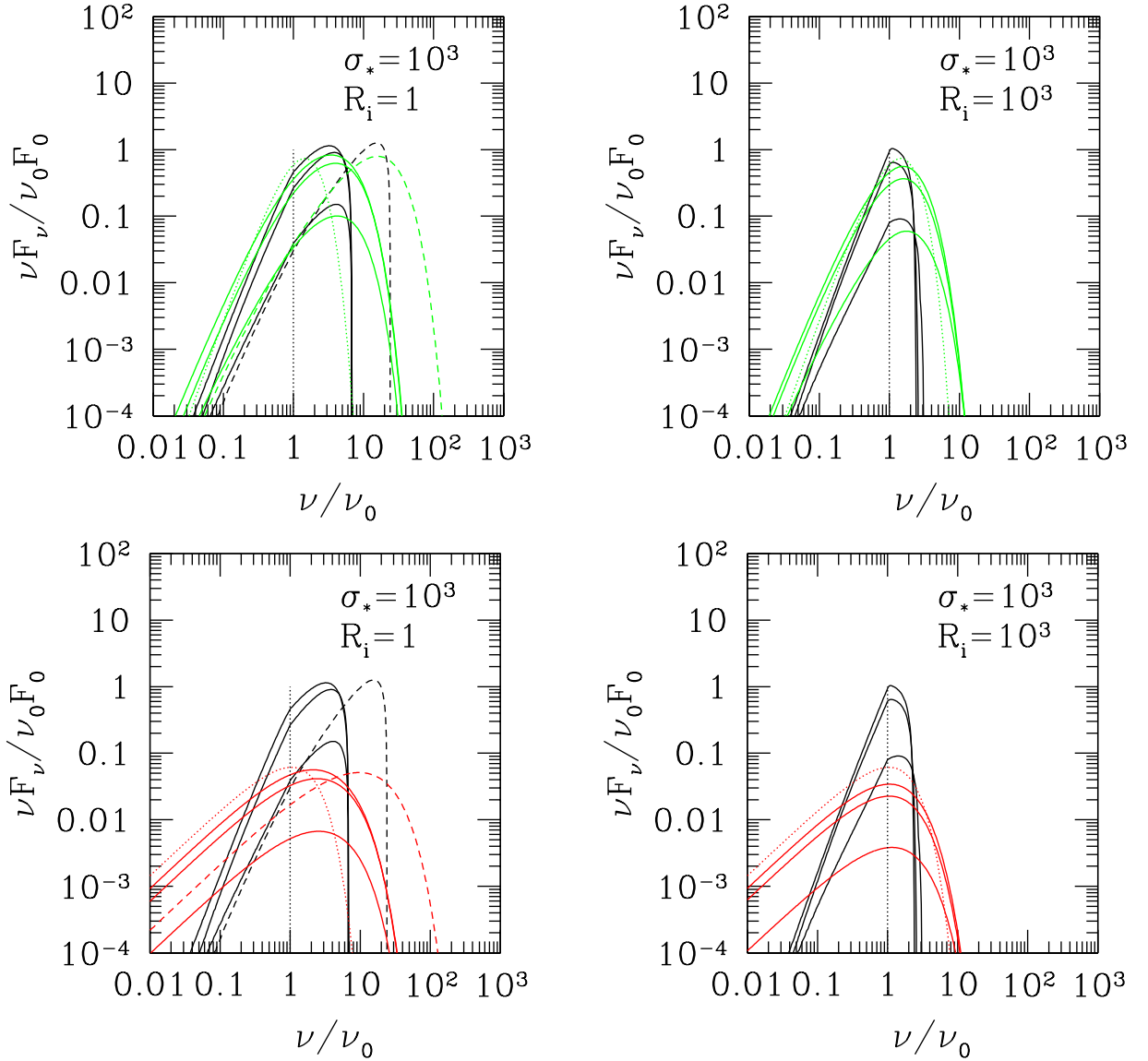


FIG. 11.— Spectra of photons emerging from a relativistic jet with a radial profile calculated by the method of Section 2, for various values of the optical depth at breakout  $\tau_{\text{es}*} = 0.1, 1, 10$  [equation (12)]. Black curves correspond to a monochromatic seed, green curves to a blackbody seed, red curves to a GRB-like seed spectrum,  $F_\nu = \text{const} \times e^{-h\nu/kT_0}$  [the lower-frequency half of the Band (1993) function extended to all frequencies]. Normalized photon energy flux at the inner radius  $r_i = 0.8r_*$ :  $\mathcal{R}_i = 1$  (left),  $\mathcal{R}_i = 10^3$  (right). Initial Lorentz factor  $\Gamma_i = 10$ . Bulk frame of the radiation field  $\Gamma_{\text{eq},i} = 10$ , except for the dashed curves which correspond to  $\Gamma_{\text{eq},i} = \Gamma_i/2 = 5$ ,  $\tau_{\text{es}*} = 0.1$ .

radiation field emerging at the jet photosphere is broader than the matter Lorentz cone: the dashed curve in the  $\mathcal{R}_i = 1$  panels is the result for  $\Gamma_{\text{eq},i} = \Gamma_i/2 = 5$  and a low optical depth ( $\tau_{\text{es}*} = 0.1$ ) at the breakout radius. As expected from the above argument, the peak of the spectrum is stretched upward in frequency above the peak of the seed spectrum.

#### 4.3. Spectrum in Jet Model II (Trans-magnetosonic)

The output spectrum is calculated by a similar method to that described in Section 4.1. The background flow is prescribed, in this case by the solutions obtained in Section 3.6, and the flow is approximated as radial. Since we are not, now, following the outflow across its photosphere, and the entire simulation volume is assumed optically thin, we take a similar input photon distribution as was used to calculate the flow acceleration: the intensity is constant,  $I = I_0$  for  $\theta < \theta_j = 0.2$  radian. The jet breakout radius is taken to be  $x_* = 3$ , as in Figure 9, and the radial optical depth  $\Delta\tau_{\text{res}}(x_i = 2, \infty, \mu = 1) = 1$ . Results are shown in Figures 12-13 for three different degrees of magnetic field flaring: strong [corresponding to  $\delta\theta = 0.3$  in equation (51)], intermediate ( $\delta\theta = 1$ ), and weak ( $\delta\theta = 10$ ). The high-energy extension of the spectrum becomes broader as the radiation compactness is

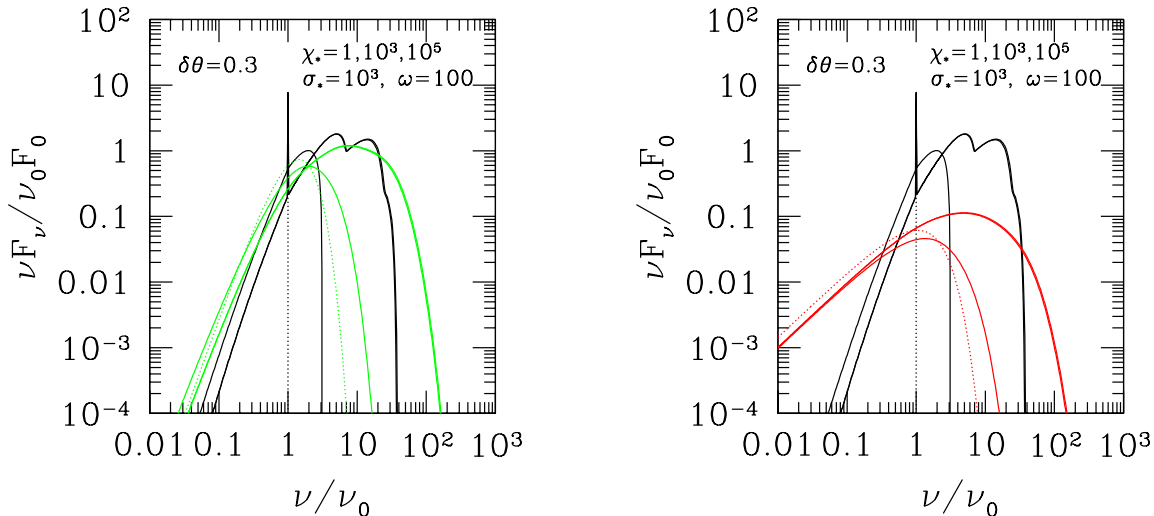


FIG. 12.— Photon spectrum emerging from a highly magnetized jet with radial profile given in Figure 9, corresponding to strong magnetic flaring [ $\delta\theta = 0.3$  in equation (51)]. The radiation compactness  $\chi_* = 1, 10^3, 10^5$  at the breakout radius  $x_* = 3$ . (The spectra extend to higher frequency at a lower compactness.) The optical depth to radially moving photons is unity at the inner boundary  $x = 2$ . Black lines: monochromatic seed spectrum. Left Panel: black-body photon source (green lines). Right Panel: GRB-like seed spectrum,  $F_\nu = \text{const} \times e^{-h\nu/kT_0}$ . Dotted curves: source spectrum.

reduced: stronger radiation drag limits the increase in  $\Gamma$  above  $\Gamma_{\text{eq}}$ . In the case of a monochromatic input spectrum, one notices the appearance of a few distinct orders of Compton scattering. The bumps in the spectrum are smoothed out when convolved with a blackbody source.

## 5. SUMMARY

We have examined the effect of intense radiation pressure on a cold, magnetized outflow with a jet geometry. The poloidal magnetic field lines are allowed to deviate from spherical symmetry, e.g. due to breakout from a confining medium. The outflow experiences a strong outward Lorentz force as a result, so that the magnetofluid and radiation field have a tendency to flow differentially outside the transparency surface. We have considered the combined dynamics of the magnetofluid and radiation, and as well as the modification to the radiation spectrum by multiple scattering.

We first considered the transition zone straddling the scattering photosphere. While the jet is still optically thick, its magnetization is suppressed by the inertia of the advected radiation. Outside the breakout point, the jet experiences a strong outward Lorentz force, which forces a rapid reduction in optical depth. This approach assumes that the fast critical surface lies deep in the jet, but calculates the radial flaring of the field lines self-consistently with a simple causal prescription, and calculates the interaction between the radiation and matter for arbitrary scattering depth.

If the jet is still optically thick at breakout, then the emergent spectrum is modestly broadened and hardened below the peak. On the other hand, breakout outside the transparency surface results in a photon beam that is significantly broader than the Lorentz cone of the accelerating jet, and therefore results in a more extended high-energy component to the spectrum. A stronger radiation field suppresses the accelerating effect of jet flaring and brings the spectrum closer to the original thermal input. Broadening of the photon beam could also be due to scattering by a shell of slower material entrained at the jet head (Thompson 2006).

Our second approach to the problem focuses on the zone outside the jet photosphere, but allows for large enough magnetization that the flow passes through the fast critical surface just outside the breakout radius. We then solve for the flow profile along magnetic flux surfaces, both inside and outside the critical point. In doing this, we choose a realistic angular distribution for the radiation field but prescribe a flaring profile for the poloidal field lines. The cross-field force balance is not solved self-consistently, but we check that in all cases the transverse component of the radiation force is small compared with the transverse Lorentz force that is implied by the chosen field profiles.

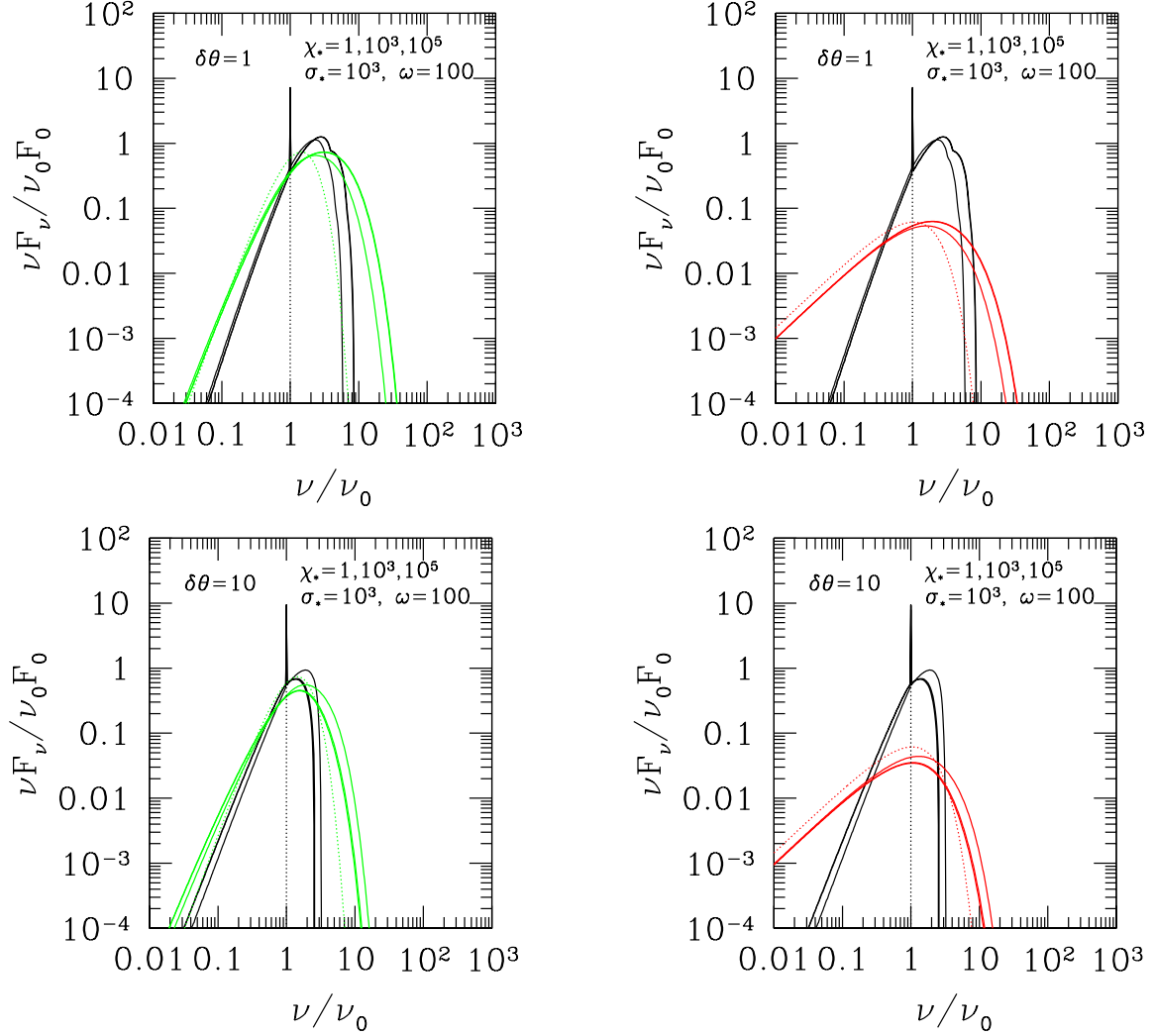


FIG. 13.— Same as 12, but with  $\delta\theta = 1 = 5\theta_j$  (top), and  $\delta\theta = 10 = 50\theta_j$  (bottom).

As regards the longitudinal motion along magnetic flux surfaces, we define the critical compactness  $\chi$  of the radiation field above which the matter and radiation are locked, and the Lorentz force is subdominant. For small jet flaring, the radiation force leads to an increase in terminal Lorentz factor at high values of  $\chi$ , but can somewhat suppress the acceleration if the flaring is strong. The extent of the high-energy component of the spectrum is shown to depend in an interesting way on the degree of flaring and the position of the photosphere relative to the breakout radius.

Issues not addressed in this paper include the effects of multiple scattering at the magnetosonic critical surface, an ambient radiation field generated far outside the engine (e.g. Li et al. 1992a; Beskin et al. 2004), or the feedback of an intense radiation flow on the poloidal structure of the magnetic field. An effect specific to gamma-ray bursts involves the sidescattering of gamma-rays outside the forward shock, combined with the radiative acceleration of the pair-enriched material up to a Lorentz factor comparable to that of the relativistic ejecta (Thompson & Madau 2000; Beloborodov 2002). This delays the deceleration of the ejecta, and makes the medium ahead of the shock optically thick to scattering (Thompson 2006). Photons side-scattered through large angles would continue to interact with jet material at a smaller radius, creating pairs downstream of the forward shock, delaying the decoupling of the photons from the jet fluid, and generating a high-energy tail to the photon spectrum by bulk Comptonization. This means that the outermost shell of jet material (of a thickness  $\sim \theta_j^2 r_*$ ) may avoid strong outward acceleration during jet breakout. However, jet material flowing at much greater distances back of the jet head sees weaker Compton drag and rates of pair creation during breakout. The slow forward shell becomes geometrically thin as it is pushed outward and, eventually, subject to a corrugation instability (Thompson 2006).

We thank the NSERC of Canada for support.

APPENDIX

GEOMETRY OF SCATTERING IN A NARROW JET

We now calculate the radiation force on plasma moving on a general trajectory within a thin jet of opening angle  $\theta_j \ll 1$ , following the setup of Section 3.1. Our goal is to obtain an analytic expression for this force, which is possible by assuming a uniform intensity  $I = \int I_\nu d\nu$  at the ‘emission’ surface (radius  $r_s$ ), and taking this surface to be locally spherical. When considering the interaction with matter, this intensity distribution gives similar results to a radiation field that is locally isotropic in the relativistic frame of the emitting medium. (See the discussion in Section 3.1 and Section 3.3 of Paper I.) The result generalizes the simpler angular momentum formalism used in Section 2 and presented in equation (24).

Photons are emitted from coordinates  $\{\theta_\gamma, \phi_\gamma\}$  within a patch of angular radius  $\theta_\gamma \leq \theta_j$ , and scatter in the jet the position  $\{x = r/r_s > 1, \theta_f, \phi_f = 0\}$ . The presence of an absorbing surface at the edge of the jet would change the radiation force at angles  $\theta_f > \theta_j$ . Given the uncertain nature of the medium outside the jet, we restrict the calculation of the force to angles  $< \theta_j$ . The photon trajectory is tilted with respect to the radial line passing through the scattering point, by an angle (Figure 14)

$$\theta_{\gamma,r} = \frac{(\theta_{\gamma,r})_s}{x-1}. \quad (\text{A1})$$

Here

$$(\theta_{\gamma,r})_s = (\theta_f^2 + \theta_\gamma^2 - 2\theta_f\theta_\gamma \cos \phi_\gamma)^{1/2} \quad (\text{A2})$$

is the corresponding angle measured on the ‘emission’ surface, and we have assumed that  $x-1 \gg \theta_j$  in making the expansion in  $x$ . The intensity at the point of scattering can then be expressed as

$$I = \int d\nu I_\nu = I_0 \quad \text{for} \quad \theta_{\gamma,r} < \sqrt{\theta_f^2 + \theta_\gamma^2 - 2\theta_f\theta_\gamma \cos \phi_\gamma} \left( \frac{r_s}{r-r_s} \right). \quad (\text{A3})$$

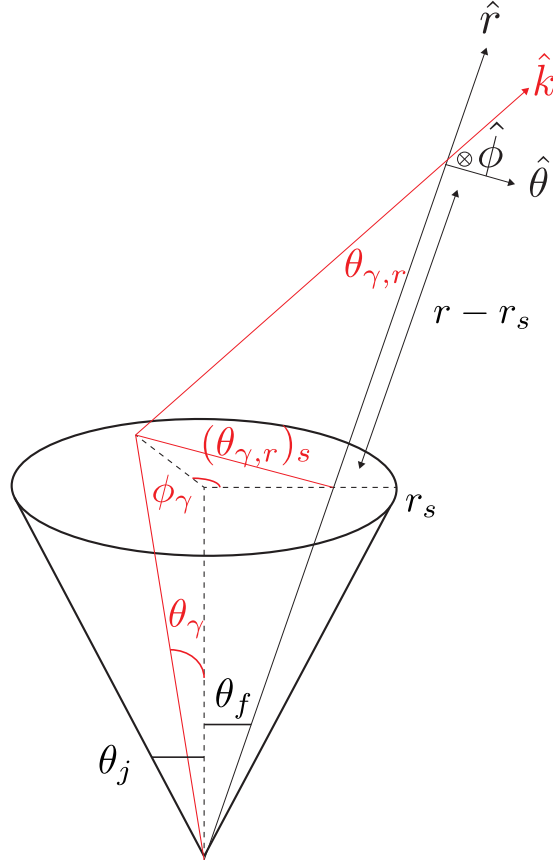


FIG. 14.— Geometry of photon emission and scattering in a thin jet. The emission surface is a circular patch of radius  $\theta_j r_s$ . We take the photon intensity to be independent of angle and uniform on this surface. Coordinates  $\{\theta_\gamma, \phi_\gamma\}$  label the point of emission, and  $\theta_{\gamma,r}$  is the angle  $\cos^{-1}(\hat{k} \cdot \hat{r})$  at the point of scattering on a field line of polar angle  $\{\theta_f, \phi_f = 0\}$ .

The unit wave vector in the local  $(\hat{r}, \hat{\theta}, \hat{\phi})$  coordinate system is

$$\hat{k} = (k_r, k_\theta, k_\phi) = \left( 1 - \frac{1}{2}\theta_{\gamma,r}^2, \frac{\theta_f - \theta_\gamma \cos \phi_\gamma}{x-1}, -\frac{\theta_\gamma \sin \phi_\gamma}{x-1} \right) \quad (\text{A4})$$

with the poloidal component

$$k_p = \frac{\beta_r}{\beta_p} k_r + \frac{\beta_\theta}{\beta_p} k_\theta = \frac{k_r + \Delta\theta_B k_\theta}{\sqrt{1 + \Delta\theta_B^2}} \simeq 1 - \frac{1}{2} \left( \frac{\theta_f}{x-1} - \Delta\theta_B \right)^2 - \frac{\theta_\gamma^2}{2(x-1)^2} + \frac{\theta_\gamma}{x-1} \left( \frac{\theta_f}{x-1} - \Delta\theta_B \right) \cos \phi_\gamma \quad (\text{A5})$$

where  $\Delta\theta_B = B_\theta/B_r$  is the angle that a bending field line makes with the local radial vector. To evaluate the lab-frame radiation force (20) we relate the solid angle of incoming photons to the emission coordinates via

$$d\Omega = \frac{\theta_\gamma}{(x-1)^2} d\theta_\gamma d\phi_\gamma. \quad (\text{A6})$$

The poloidal and toroidal radiation force is then evaluated as follows. We begin by writing

$$1 - \beta \cdot \hat{k} = A + B \cos \phi_\gamma + C \sin \phi_\gamma \quad (\text{A7})$$

and express the components of the wave vector as

$$\hat{\beta}_{p,\phi} \cdot \hat{k} = D_{p,\phi} + E_{p,\phi} \cos \phi_\gamma + F_{p,\phi} \sin \phi_\gamma. \quad (\text{A8})$$

Integrating first over  $\phi_\gamma$  and then  $\theta_\gamma$  at the ‘emission’ surface gives

$$F_{p,\phi}^{\text{rad}} = \frac{\sigma_T I}{c(x-1)^2} \int_0^{\theta_j} d\theta_\gamma \theta_\gamma [2\pi A D_{p,\phi} + \pi B E_{p,\phi} + \pi C F_{p,\phi} - \beta_{p,\phi} \Gamma^2 (2\pi A^2 + \pi B^2 + \pi C^2)] \quad (\text{A9})$$

$$= \frac{\bar{m}c^2}{r_s} \chi_* \frac{(x_* - 1)^2}{x_* (x-1)^2} \left[ \frac{1}{2} G_{p,\phi} + \frac{1}{4} \theta_j^2 H_{p,\phi} + \frac{1}{6} \theta_j^4 K_{p,\phi} \right] \quad (\text{A10})$$

with

$$G_p \simeq 2(1 - \beta_p) [1 - \beta_p \Gamma^2 (1 - \beta_p)] - \frac{1}{2} \beta_p (1 + \beta_p^2 \Gamma^2) \left( \frac{\theta_f}{x-1} - \Delta\theta_B \right)^4 \quad (\text{A11})$$

$$H_p \simeq -\frac{\beta_p^3 \Gamma^2}{(x-1)^2} \left[ 2 \left( \frac{\theta_f}{x-1} - \Delta\theta_B \right)^2 + \frac{\beta_\phi^2}{\beta_p^2} \right] \quad (\text{A12})$$

$$K_p = -\frac{\beta_p}{2(x-1)^4} (1 + \beta_p^2 \Gamma^2). \quad (\text{A13})$$

$$G_\phi = -2\beta_\phi \Gamma^2 \left[ (1 - \beta_p)^2 + \beta_p (1 - \beta_p) \left( \frac{\theta_f}{x-1} - \Delta\theta_B \right)^2 + \frac{1}{4} \beta_p^2 \left( \frac{\theta_f}{x-1} - \Delta\theta_B \right)^4 \right] \quad (\text{A14})$$

$$H_\phi = -\frac{\beta_\phi}{(x-1)^2} \left[ 1 + \Gamma^2 (2\beta_p(1 - \beta_p) + \beta_\phi^2) + 2\beta_p^2 \Gamma^2 \left( \frac{\theta_f}{x-1} - \Delta\theta_B \right)^2 \right] \quad (\text{A15})$$

$$K_\phi = -\frac{\beta_\phi \beta_p^2 \Gamma^2}{2(x-1)^4} \quad (\text{A16})$$

where  $G_p$  and  $H_p$  are accurate to first order in  $\Gamma^{-2}$  and  $(\theta/x)^2$ . The equilibrium Lorentz factor of the photon field, the frame in which  $\mathbf{F}^{\text{rad}}$  vanishes, is found by solving  $\Gamma'_\chi = 0$  in (47). The results are shown in Figure 15 for the poloidal field line profile described in Sec. 3.2. At a radius  $x-1 \gg \theta_j$  one finds  $\Gamma_{\text{eq}} \simeq x/\theta_j$ , with a coefficient of order unity that depends on the footprint angle and flaring profile. A thin jet defines a relativistic frame at relatively small distances from the ‘emission’ surface, as compared with a spherically symmetric outflow (for which  $\Gamma_{\text{eq}} \simeq 3^{1/4}x$ ). Photons arriving at a scattering point from large angles provide relatively strong drag.

The jet fluid maintains rapid rotation around the light cylinder,  $\theta_f \sim 1/x\omega$ , where the fluid flow is less aligned with the radiation field and  $\Gamma_{\text{eq}}$  is reduced. Estimating  $\beta_\phi \simeq 1/x\omega\theta_f$  (just outside the light cylinder), one finds

$$\Gamma_{\text{eq}} \simeq \left( \frac{\theta_j^4}{3(x-1)^4} + \frac{1}{x^4 \omega^4 \theta_f^4} \right)^{-\frac{1}{4}}, \quad (\text{A17})$$

valid for all  $x$ .

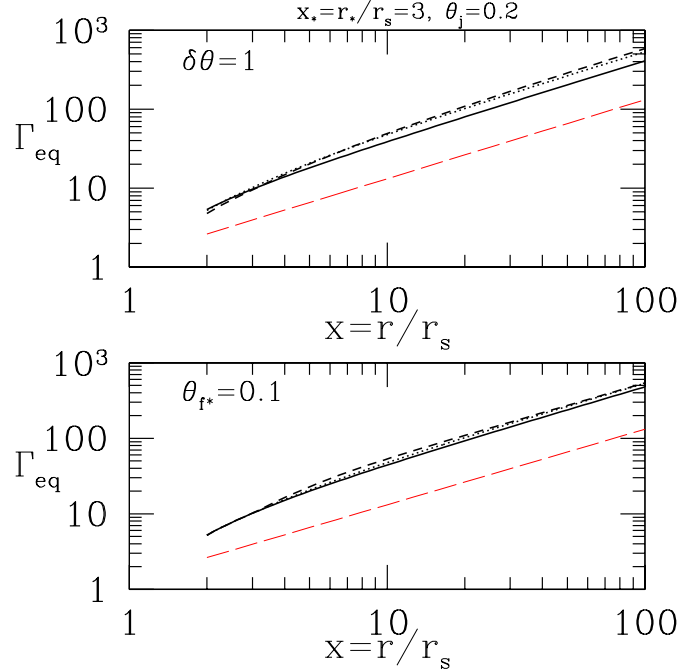


FIG. 15.— Lorentz factor at which material in a thin jet ( $\theta_j = 0.2$ ) feels a vanishing radiation force  $\mathbf{F}^{\text{rad}}$ . *Upper panel:* Moderately flared magnetic field [ $\delta\theta = 1$  in equation (51)], with black lines corresponding to different footprints at the breakout radius:  $\theta_{f*} = 0.05, 0.1, 0.15$  (solid, dotted and dashed). *Lower panel:* Different degrees of magnetic flaring,  $\delta\theta = 10, 1, 0.3$  (weak, medium, strong flaring) for a field line anchored at  $\theta_{f*} = 0.1$ . Long-dashed red line:  $\Gamma_{\text{eq}}$  for a spherical emission surface and monopolar poloidal field.

#### ACCOUNTING FOR ROTATION OF THE PHOTON FIELD

The photon source rotates rapidly in some cases, e.g. a rapidly rotating star such as a millisecond magnetar, or the merged remnant of a white dwarf binary. We can approximate the effect of a rotating emission surface by setting

$$\beta_\phi \rightarrow \beta_\phi - \frac{\beta_{\phi,R}}{x\theta_f} \quad (\text{B1})$$

in equations (43). Here  $\beta_{\phi,R}$  is a constant representing the aberration of the outflowing photons at  $r = r_s$  ( $x = 1$ ). In this situation, plasma near the emission surface can more easily co-rotate with the radiation field while still being accelerated outward.

The value of  $\beta_{\phi,R}$  depends on the type of source. One has  $\beta_{\phi,R} \sim \Omega r_s / c \equiv \omega$  when the photons flow from the surface of a star of radius  $r_s$  through a transparent wind. On the other hand, if the outflow is optically thick in a narrow radial zone close to the engine, then one expects  $\beta_{\phi,R} \sim (\Omega r_s / c)^{-1} \sim \omega^{-1}$  based on the conservation of angular momentum from the light cylinder out to the transparency surface ( $x = 1$ ).

#### WIND EQUATIONS FOR JET MODEL II

Here we derive the equations (46)-(50) for the longitudinal development of Lorentz factor and particle angular momentum along magnetic flux surfaces. Beginning with the poloidal and toroidal components of the Euler equation, (41) and (42), we expand the derivatives on the right hand side as

$$\partial_l (r\theta B_\phi) = B_\phi \partial_l (r\theta_f) + r\theta \frac{B_\phi}{B_r} \partial_l B_r + r\theta_f B_r \partial_l \left( \frac{B_\phi}{B_r} \right). \quad (\text{C1})$$

This can be evaluated using  $\partial_l (r\theta_f) \simeq \theta_f + B_\theta / B_r = \theta_f + \Delta\theta_B$ , equation (39) for  $\partial_l B_r$ , and

$$v_r \partial_l \left( \frac{B_\phi}{B_r} \right) = \partial_l v_\phi \left( 1 + \frac{v_\phi B_\phi}{v_r B_r} \right) - \frac{B_\phi}{B_r} \frac{\partial_l \Gamma}{v_r \Gamma^3} - \Omega_f (\theta_f + \Delta\theta_B), \quad (\text{C2})$$

where

$$\frac{\partial_l v_\phi}{v_\phi} = \frac{\partial_l \mathcal{L}_m}{\mathcal{L}_m} - \frac{1}{r} \left( 1 + \frac{\Delta\theta_B}{\theta_f} \right) - \frac{\partial_l \Gamma}{\Gamma}. \quad (\text{C3})$$

The wind equations (41), (42) are now transformed into ordinary differential equations by ignoring the cross-field force balance:

$$\left[ 1 - \frac{\sigma}{(x\theta_f\omega)^2 \Gamma} \left( \beta_\phi \Lambda + \frac{1}{\beta_r \Gamma^2} \frac{B_\phi}{B_r} \right) \frac{B_\phi}{B_r} \right] \frac{d\Gamma}{dl} - \frac{1}{x\theta_f} \left[ \beta_\phi - \frac{\sigma}{(x\theta_f\omega)^2 \Gamma} \frac{B_\phi}{B_r} \Lambda \right] \frac{d\mathcal{L}_m}{dl} = \frac{\sigma \Psi}{(x\theta_f\omega)^2} \frac{B_\phi}{B_r} + \chi_* R_j; \quad (\text{C4})$$

$$\frac{\sigma}{(x\theta_f\omega)^2\Gamma} \left( \beta_\phi\Lambda + \frac{1}{\beta_r\Gamma^2} \frac{B_\phi}{B_r} \right) \frac{d\Gamma}{dl} + \frac{1}{x\theta_f} \left[ \beta_r - \frac{\sigma}{(x\theta_f\omega)^2\Gamma} \Lambda \right] \frac{d\mathcal{L}_m}{dl} = -\frac{\sigma\Psi}{(x\theta_f\omega)^2} + \chi_* P_j, \quad (C5)$$

where

$$\Lambda \equiv 1 + \frac{\beta_\phi}{\beta_r} \frac{B_\phi}{B_r}; \quad \Psi \equiv \left( 1 + \frac{\Delta\theta_B}{\theta_f} \right) (1 + \Lambda) \frac{\beta_\phi}{x} + \frac{B_\phi}{B_r} \frac{\beta_r}{A} \frac{dA}{dl}. \quad (C6)$$

Two simple tests of these equations are made possible by neglecting the radiation force. The energy and angular momentum integrals (38) are now related by

$$\frac{d\Gamma}{dl} - \omega \frac{d\mathcal{L}_m}{dl} = 0. \quad (C7)$$

This equation is recovered by summing (C4) and  $B_\phi/B_r$  times (C5), and making use of Ferraro's law (4). Second, outside the fast point the inertia of the magnetofluid is dominated by the matter: the coefficient of  $d\Gamma/dl$  in equation (C4) is  $\simeq 1 - \sigma/\Gamma^3$  and approaches unity. Since in addition  $\beta_\phi \rightarrow 0$ , the term involving  $\mathcal{L}_m$  can be neglected and one finds

$$\frac{d\Gamma}{dl} \simeq \frac{\sigma_*}{A^2} \frac{dA}{dl} \quad (\Gamma^3 \gg \sigma). \quad (C8)$$

The same result can be obtained from the integral equations (8), (38) and (39),

$$\Gamma = \Gamma_* + \sigma_* (1 - A^{-1}). \quad (C9)$$

Equation (46) is then obtained by solving (C4) and (C5) for  $d\Gamma/dl$  and  $d\mathcal{L}_m/dl$ .

#### CROSS-FIELD FORCES

Though we ignore the cross-field force balance, it is useful to estimate the transverse radiation force and compare it with the Lorentz force that is implied by a given field-line profile. Our procedure becomes inconsistent if the transverse radiation force dominates, because the radiation field will then comb out the field lines in the radial direction.

The polar component of equation (20) gives the estimate,

$$F_\theta^{\text{rad}} \simeq \frac{\bar{m}c^2}{r_s} \chi_* \frac{(x_* - 1)^2}{2x_*(x - 1)^2 \Gamma^2} \left( \frac{\theta_f}{x - 1} - \frac{1}{2} \Delta\theta_B \right). \quad (D1)$$

The first term on the right-hand side represents the force imparted by photons streaming from a finite polar cap toward particles on off-axis field lines. The second represents the drag imparted as the poloidal particle flow bends across the radiation field. The cross-field Lorentz force is given by

$$\frac{\bar{m}}{4\pi\rho} [(\nabla \times \mathbf{B}) \times \mathbf{B}]_\theta \simeq \frac{\bar{m}B_\phi^2}{4\pi\rho r\theta_f} = \bar{m}c^2 \frac{\sigma}{r\theta_f}. \quad (D2)$$

Requiring this to be greater than (D1) gives an upper bound on the radiation compactness at jet breakout ( $x > x_* \gg 1$ ),

$$\frac{\chi_*}{\sigma} < \frac{2x\Gamma^2}{x_*\theta_f} \left( \frac{\theta_f}{x} - \frac{\Delta\theta_B}{2} \right)^{-1}. \quad (D3)$$

Our calculations can admit values of  $\chi_*$  as large as  $\sim 10^4\sigma$  without any inconsistency, given the typical jet parameters  $\theta_j \sim 0.2$ ,  $x_* \sim 3$ ,  $\Gamma > \Gamma_* \sim 10$ .

#### REFERENCES

- Amati, L., Frontera, F., Tavani, M., et al. 2002, *A&A*, 390, 81  
Band, D., Matteson, J., Ford, L., et al. 1993, *ApJ*, 413, 281  
Begelman, M. C., & Li, Z.-Y. 1994, *ApJ*, 426, 269  
Beloborodov, A. M. 2002, *ApJ*, 565, 808  
Beloborodov, A. M. 2010, *MNRAS*, 407, 1033  
Beloborodov, A. M. 2011, *ApJ*, 737, 68  
Beskin, V. S., Zakamska, N. L., & Sol, H. 2004, *MNRAS*, 347, 587  
Beskin, V. S., & Nokhrina, E. E. 2006, *MNRAS*, 367, 375  
Camenzind, M. 1987, *A&A*, 184, 341  
Dessart, L., Ott, C. D., Burrows, A., Rosswog, S., & Livne, E. 2009, *ApJ*, 690, 1681  
Drenkhahn, G., & Spruit, H. C. 2002, *A&A*, 391, 1141  
Ferraro, V. C. A. 1937, *MNRAS*, 97, 458  
Giannios, D. 2006, *A&A*, 457, 763  
Giannios, D., & Spruit, H. C. 2007, *A&A*, 469, 1  
Goldreich, P., & Julian, W. H. 1970, *ApJ*, 160, 971  
Kiusalaas, J. 2010, *Numerical Methods in Engineering with Python* (2nd ed.; New York: Cambridge University Press)  
Kulkarni, S. R., Djorgovski, S. G., Odewahn, S. C., et al. 1999, *Nature*, 398, 389  
Li, Z.-Y., Begelman, M. C., & Chiueh, T. 1992, *ApJ*, 384, 567  
Li, Z.-Y., Chiueh, T., & Begelman, M. C. 1992, *ApJ*, 394, 459L  
London, R. A., & Flannery, B. P. 1982, *ApJ*, 258, 260  
MacFadyen, A. I., & Woosley, S. E. 1999, *ApJ*, 524, 262  
Meszaros, P., & Rees, M. J. 1997, *ApJ*, 482, L29  
Michel, F. C. 1969, *ApJ*, 158, 727  
Paczynski, B. 1998, *ApJ*, 494, L45  
Rees, M. J., & Mészáros, P. 2005, *ApJ*, 628, 847  
Russo, M., & Thompson, C., *ApJ*, submitted  
Tehekovskoy, A., McKinney, J. C., & Narayan, R. 2009, *ApJ*, 699, 1789  
Tehekovskoy, A., Narayan, R., & McKinney, J. C. 2010, 15, 749  
Thompson, C. 1994, *MNRAS*, 270, 480  
Thompson, C. 2006, *ApJ*, 651, 333  
Thompson, C., & Madau, P. 2000, *ApJ*, 538, 105  
Vlahakis, N., & Königl, A. 2003, *ApJ*, 596, 1080  
Vlahakis, N., & Königl, A. 2003, *ApJ*, 596, 1104  
Woosley, S. E. 1993, *ApJ*, 405, 273  
Zhang, B., & Yan, H. 2011, *ApJ*, 726, 90